The influence of biogenic opal on ^{231}Pa/^{230}Th in sediments from the Bermuda Rise and its implication for paleocirculation reconstructions

A Thesis Presented

by

Theresa Marie King

to

The Graduate School

in Partial Fulfillment of the

Requirements

for the Degree of

Master of Science

in

Marine and Atmospheric Science

Stony Brook University

August 2014

Stony Brook University

The Graduate School

Theresa Marie King

We, the thesis committee for the above candidate for the

Master of Science degree, hereby recommend

acceptance of this thesis.

David E. Black – Thesis Advisor
Associate Professor, School of Marine and Atmospheric Sciences

J. Kirk Cochran – Second Reader
Professor, School of Marine and Atmospheric Sciences

Charles N. Flagg – Third Reader
Research Professor, School of Marine and Atmospheric Sciences

This thesis is accepted by the Graduate School

Charles Taber
Dean of the Graduate School

Abstract of the Thesis

The influence of biogenic opal on ^{231}Pa/^{230}Th in sediments from the Bermuda Rise and its implication for paleocirculation reconstructions

by

Theresa Marie King

Master of Science

in

Marine and Atmospheric Science

Stony Brook University

2014

Thermohaline circulation is responsible for the global transport of heat in surface waters of the ocean, and variability in this circulation has been linked to both short- and long-term climate change on time scales ranging from centuries to tens of thousands of years. Accurate reconstructions of past variability are thus critical to understanding modern and future thermohaline circulation changes and the response of the global climate system. The main circulation feature in the Atlantic is Atlantic Meridional Overturning Circulation (AMOC), and has been reconstructed using a variety of static proxies, but more recently through the use of sedimentary ^{231}Pa$_{xs}$/^{230}Th$_{xs}$. The ratios of these radionuclides through time provide a relative rate of circulation based on the uneven scavenging efficiencies of ^{231}Pa and ^{230}Th in the water column, and hence provide a measure of the speed at which the waters flow through the Atlantic basin. However, the ^{231}Pa$_{xs}$/^{230}Th$_{xs}$ proxy has been shown to inaccurately depict AMOC variability when biogenic opal comprises a significant component of the overall particle flux.

This study will present the biogenic opal and ^{231}Pa$_{xs}$/^{230}Th$_{xs}$ records preserved in Bermuda Rise sediments for the majority of the Holocene epoch (~9 kya–present, based on radiocarbon-dated planktonic foraminifera). The location of the Bermuda Rise and its extremely high sedimentation rate allow for millennial-scale sampling resolution to examine the relationship between biogenic opal flux and sedimentary ^{231}Pa$_{xs}$/^{230}Th$_{xs}$. Stable oxygen and carbon isotope data from planktonic foraminifera will also provide a climate context for the sediment record.

Results reveal a significant correlation ($p < 0.05$) between $^{230}Th_{xs}$-normalized opal flux and $^{231}Pa_{xs}/^{230}Th_{xs}$ through the Holocene, but the statistical significance is driven by the sample taken at the core-top. Without this sample the records are no longer significantly correlated ($p > 0.05$), supporting the use of $^{231}Pa_{xs}/^{230}Th_{xs}$ as a proxy for paleocirculation at the Bermuda Rise over the interval of study minus the surface layer. The surface sample-driven correlation implies that there is a compositional effect of biogenic opal in the most recently-deposited sediments, a hypothesis supported by a benthic foraminiferal $\delta^{13}C$ record of a nearby core. It is unclear at this time whether the increase in opal flux was produced locally or the result of lateral silica transport to the Bermuda Rise. The surface samples are also characterized by a bioturbated mixed layer which muted the signal of well-known Holocene climate events such as the Little Ice Age (~400 ybp) and the Medieval Climate Anomaly (~1 kya).

Interpretation of the remainder of the $^{231}Pa_{xs}/^{230}Th_{xs}$ record as unbiased changes of AMOC variability indicate that circulation through the Holocene was relatively stable with the exception of an interval of slightly weakened circulation from ~5700–4100 ybp. Although comparisons with several other paleocirculation proxies from nearby Bermuda Rise cores were ambiguous, it is beneficial to learn that $^{231}Pa_{xs}/^{230}Th_{xs}$ ratios are a reliable proxy through the majority of the Holocene at this site.

Table of Contents

List of Figures....vi
List of Tables....vii
List of Abbreviations....viii
Acknowledgements....ix
Introduction....1
    Thesis Objectives....1
    Atlantic Meridional Overturning Circulation....1
    Proxies for AMOC Reconstructions....3
        Static Proxies....3
        Kinematic Proxies....4
    $^{231}Pa_{xs}/^{230}Th_{xs}$....5
        Influence of Particle Composition....6
Study Site....9
    Formation and Setting....9
    Sediment Characteristics....10
    Previous Studies....12
        Paleonutrient-Based Reconstructions of AMOC....12
        $^{231}Pa_{xs}/^{230}Th_{xs}$-Based Reconstructions of AMOC....15
Materials and Methods....19
    Sediment Sampling....19
    Biogenic Opal Analysis....19
    Stable Isotope Analysis....20
    Age Model....21
    Radionuclide Analysis....25
    $^{230}Th_{xs}$ Normalization....30
Results....32
    Sedimentation Rates....32
    Stable Oxygen Isotopes....32
    Stable Carbon Isotopes....35
    Biogenic Opal Flux....37
    Sedimentary $^{231}Pa_{xs}/^{230}Th_{xs}$....39
Discussion....41
    Determination of Biogenic Opal Effect on Sedimentary $^{231}Pa_{xs}/^{230}Th_{xs}$....41
    Interpretations of AMOC Changes through the Holocene....52
    Holocene Climate Variability from BR-MC2 Sediments....56
Conclusions....59
References....61
Appendix I....66
Appendix II....69
Appendix III....70
Appendix IV....73

List of Figures

Figure 1: Location of Bermuda Rise and core BR-MC2 11
Figure 2: Age model based on ^{14}C dated depths throughout core 24
Figure 3: Mass accumulation rates for sediment and biogenic opal plotted with supplemented $^{230}Th_{xs}$-normalized sediment and opal fluxes 31
Figure 4: Supplemented $^{230}Th_{xs}$-normalized sediment flux 33
Figure 5: Planktic $\delta^{18}O$ for BR-MC2 with 9-point running average 34
Figure 6: Planktic $\delta^{13}C$ for BR-MC2 with 9-point running average 36
Figure 7: %Opal for BR-MC2 plotted with supplemented $^{230}Th_{xs}$-normalized opal flux 38
Figure 8: Supplemented $^{231}Pa_{xs}/^{230}Th_{xs}$ record 40
Figure 9: Supplemented $^{231}Pa_{xs}/^{230}Th_{xs}$ record plotted against supplemented $^{230}Th_{xs}$-normalized opal flux. Scatter plots with and without surface sample determine correlation 45
Figure 10: Supplemented $^{231}Pa_{xs}/^{230}Th_{xs}$ record plotted against supplemented $^{230}Th_{xs}$-normalized sediment flux. Scatter plots with and without surface sample determine correlation 46
Figure 11: BR-MC2 $^{231}Pa_{xs}/^{230}Th_{xs}$ record plotted against $^{230}Th_{xs}$-normalized opal flux. Scatter plots with and without surface sample determine correlation 48
Figure 12: BR-MC2 $^{231}Pa_{xs}/^{230}Th_{xs}$ record plotted against $^{230}Th_{xs}$-normalized sediment flux. Scatter plots with and without surface sample determine correlation 49
Figure 13: Planktic $\delta^{13}C$ for BR-MC2 (with 9-point running average) plotted with supplemented $^{230}Th_{xs}$-normalized opal flux 51
Figure 14: Supplemented $^{231}Pa_{xs}/^{230}Th_{xs}$ record plotted with benthic $\delta^{13}C$ from nearby cores to compare marked intervals of increased $^{231}Pa_{xs}/^{230}Th_{xs}$ 53
Figure 15: Benthic Cd/Ca record from nearby cores plotted with Planktic $\delta^{18}O$ for BR-MC2 (with 9-point running average) to compare marked intervals of increased $^{231}Pa_{xs}/^{230}Th_{xs}$ 55
Figure 16: Planktic $\delta^{18}O$ for BR-MC2 (with 9-point running average) marked with climate events of the Holocene 58

List of Tables

Table 1: Radiocarbon dated samples with their respective raw ^{14}C ages and calibrated years before present 23

List of Abbreviations

AABW	Antarctic Bottom Water
Al	Aluminum
AMOC	Atlantic Meridional Overturning Circulation
^{12}C	Carbon-12
^{14}C	Carbon-14
Cd/Ca	Cadmium/Calcium
cm	Centimeter
δ^{13}C	Delta Carbon-13
δ^{18}O	Delta Oxygen-18
$FeCl_3$	Iron (III) Chloride
g	Gram
GNAIW	Glacial North Atlantic Intermediate Water
H1	Heinrich 1
HCl	Hydrochloric Acid
$HClO_4$	Perchloric Acid
HF	Hydrofluoric Acid
HNO_3	Nitric Acid
K_d	Partition Coefficient
km	Kilometer
kya	Thousand Years Ago
kyr	Thousand Years
LGM	Last Glacial Maximum
LIA	Little Ice Age
m	Meter
MCA	Medieval Climate Anomaly
µg	Microgram
µm	Micrometer
MIS	Marine Isotope Stage
mL	Milliliter
mM	Millimolar
M	Molar
N	Normal
Na_2CO_3	Sodium Carbonate
NADW	North Atlantic Deep Water
NH_4OH	Ammonium Hydroxide
ODP	Ocean Drilling Program
^{231}Pa	Protactinium-231
^{233}Pa	Protactinium-233
$^{231}Pa_{xs}$	Excess Protactinium-231
R/V	Research Vessel
Si	Silica
^{229}Th	Thorium-229
^{230}Th	Thorium-230
$^{230}Th_{xs}$	Excess Thorium-230
^{234}U	Uranium-234
^{235}U	Uranium-235
^{236}U	Uranium-236
^{238}U	Uranium-238
ybp	Years Before Present
YD	Younger Dryas
yr	Years

Acknowledgments

My success here at SoMAS is due in large part to the support and guidance I received along the way. It seemed like a very long three years, but I've finally made it through with the help of so many people.

First and foremost, I would like to thank my advisor, Dave. Not only did he provide guidance through my research, but he has helped me figure out what my goals are after a Master's degree. Working with Dave has allowed me many opportunities to work with a variety of people in a variety of places, and for that I am truly grateful.

I would also like to acknowledge my other committee members, Kirk and Charlie. They have provided comments and questions throughout this process that have helped developed my thesis research.

Another person instrumental to this research was Patrick Fitzgerald. He has helped me make my way through the world of radioisotopes and I could not have completed this work without him, I owe him many thanks. I would also like to thank Jennifer Wurtzel and Kristen Butler. As fellow members of the Paleoceanography and Paleoclimatology Lab we spent hours together in the lab and they taught me how to successfully wash and pick forams, and spent some of their own time working on my samples.

I am also extremely grateful for the friends I have made here at Stony Brook University. They have all given me support, encouragement, or just lent an ear if I had a long day. In particular I would like to thank Beth Cummins, Kaylyn Marsano, Casey Griffin, Rebecca Kulp, Laura Treible, and Kellie McCartin. I appreciate all of the time we spent together, and the adventures we had. These people, among many others really made my time at SBU more enjoyable.

My family has also offered me unyielding support in all of my endeavors and I am extremely grateful for them. My parents have always been excited about what I decide to do and have supported each decision I make. My stepmother, Carole, has also offered her support and I would not be where I am without the guidance that she and my parents have provided. My siblings, Vicki, Stephen, and Abby, have always been there for me and I am thankful for their love and support. They are an entertaining bunch when we get together, and have really kept me sane through this journey.

Lastly, I would like to thank my fiancé, Justin. I am especially grateful for his enduring support through graduate school. He has been there for me after many long, difficult days in the lab, and listened to every little thing that had gone wrong; and just as important, he's been excited for me after something as simple as making sense of a figure. He's given me advice and countless encouraging words over the years and I am immensely grateful for him.

Introduction

This chapter presents background information and motivations to understand the analyses and implications of this study.

Thesis Objectives

The goal of this project is to better understand the influence of biogenic opal flux on sedimentary $^{231}Pa/^{230}Th$ at the Bermuda Rise. $^{231}Pa/^{230}Th$ is a widely used proxy for past ocean circulation, but is largely influenced by particle flux and composition (Anderson et al., 1983; Walter et al., 1997). Biogenic opal can decrease the fractionation of radioisotopes in the water column, resulting in a sediment record that does not accurately reflect the rate of circulation at the time of deposition (Chase et al., 2002; Roberts et al., 2009). This study examines the Bermuda Rise sediment record over the last ~9 kyr to explore possible relationships between the flux of biogenic opal and sedimentary $^{231}Pa/^{230}Th$, allowing for increasingly accurate future reconstructions of Atlantic Meridional Overturning Circulation.

Atlantic Meridional Overturning Circulation

Global climate is controlled to a significant extent by the world's oceans through the circulation of heat. Stored in the surface waters, heat is transported poleward and emitted into the atmosphere increasing temperatures and affecting global climate and weather conditions (Lopes dos Santos et al., 2010). In the Atlantic Ocean, the main circulation feature is known as Atlantic Meridional Overturning Circulation (AMOC), characterized by relatively low-density warm surface waters flowing north along the western boundary of the Atlantic where they release heat, become increasingly dense, and sink to flow south at depth (Lynch-Stieglitz et al., 2007). This system creates a net transport of heat northward instead of symmetrically-poleward, therefore any alterations in the rate of overturning would significantly impact climate on a hemispheric or global scale (Vellinga and Wood, 2002).

It has been observed in sediment proxy data that a weakened state of AMOC existed during the Last Glacial Maximum (LGM, ~20 kya), linking colder climate to reduced AMOC and overall heat transport (Curry and Oppo, 2005; Lynch-Stieglitz et al., 2007). Such links exist not only for long periods of time like glacial and interglacial periods, but also for smaller-scale, short-term climate events. Climate models from Vellinga and Wood (2002) show that a total shut-down of AMOC (which evidence indicates has happened during Heinrich events ~17 kya; McManus et al., 2004) would result in warming surface air temperatures in the South Atlantic of ~1 ºC, and up to 8 ºC cooling in the North Atlantic in the span of only three decades. These temperature anomalies would be accompanied by shifts in overall evaporation and precipitation patterns around both the North and South Atlantic basins (Vellinga and Wood, 2002).

In addition to heat transport, the deep currents formed by AMOC circulate ventilated waters to depth, removing carbon from the atmosphere and storing it in the deep ocean (Negre et al., 2010). This bipolar seesaw of surface waters and storage of greenhouse gases emphasizes our need to better understand the role of AMOC with respect to climate events through history (Broecker, 2000). Without accurate knowledge of how past ocean circulation has varied through time it is difficult to project what circulation patterns will result from modern and future climate changes.

Proxies for AMOC Reconstructions

There are two types of proxies for assessing past ocean circulation: static and kinematic. Static proxies use chemical tracers to determine the relative proportions and positions of water masses present at the depth of interest whereas kinematic proxies provide information as to the rates of circulation (Henderson, 2002).

Static Proxies

The most commonly used static proxies include benthic foraminiferal $\delta^{13}C$ and Cd/Ca ratios. Water masses have a certain level of nutrients based on their formation and age, reflected by characteristic $\delta^{13}C$ and Cd/Ca values recorded in the calcite tests of foraminifera. Waters enriched in nutrients exhibit a lower $\delta^{13}C$ as they contain proportionately higher levels of ^{12}C, creating a lighter reservoir of inorganic carbon from which foraminifera create calcite shells. These high-nutrient waters also exhibit high Cd/Ca ratios as Cd is a micronutrient for foraminifera and correlates strongly with PO_4^{-3} in the water column (Henderson, 2002).

In the modern Atlantic Ocean, Antarctic Bottom Water (AABW) is formed from upwelled, nutrient-rich waters. Over time, primary production uses up the lighter carbon and depletes the nutrients. However, as AABW sinks and ages, organic matter is remineralized, releasing nutrients and a relative excess of ^{12}C into the surrounding water resulting in characteristically low $\delta^{13}C$ and high Cd/Ca signature. In contrast, North Atlantic Deep Water (NADW) is formed in large part by nutrient-poor surface waters that lack substantial primary production, allowing NADW to retain its relatively high $\delta\ ^{13}C$ and low Cd/Ca values (Lynch-Stieglitz et al., 2007). The biogeochemical signals can then be interpreted as the relative geometry of deep water masses (i.e. a signal characteristic of AABW at northern latitudes would indicate a weakened AMOC at that time, where decreased production of NADW allows AABW to flow further north and fill the deep basin).

Complications have been noted with $\delta^{13}C$ in that an increased rain rate of organic carbon can cause benthic foraminifera to reflect a $\delta^{13}C$ lower than the actual dissolved inorganic carbon content of the water mass. However, this has only been a problem at sampling sites that lie beneath productive surface waters (Mackensen et al., 2001).

Kinematic Proxies

Kinematic proxies are increasingly useful as they reflect rates of circulation as opposed to relative water mass proportions. Such proxies include sediment grain size, radiocarbon dating of seawater dissolved inorganic carbon, and the ratio of the radionuclides ^{231}Pa to ^{230}Th. Sea floor sediment grain size is independent of sediment supply and is a direct product of the speed of deep water flow and thus provides data as to how rapidly water moves over the sampling site. Faster flow/higher energy causes the erosion of smaller particles leaving behind an average larger sediment grain size. The opposite holds true as smaller mean sediment size is an indication of reduced flow rate (Bianchi and McCave, 1999).

Radiocarbon is a kinematic proxy that provides circulation rates in terms of years as opposed to relative flow rates. This is done through determining the ages of bottom water masses, and by extension, their ventilation (or time since last at the surface). ^{14}C ages of benthic and planktonic foraminifera in the same sample are measured - the difference between them is the age difference between surface waters and deep waters and indicates how long the water mass has been away from the surface (Matsumoto, 2007).

$^{231}Pa/^{230}Th$

^{231}Pa and ^{230}Th are daughter isotopes of naturally occurring ^{235}U and ^{234}U, respectively. Uranium is found uniformly through the world's oceans and decays to produce ^{231}Pa (half-life of 32,500 years) and ^{230}Th (half-life of 75,000 years) at a constant activity ratio of (^{231}Pa/^{230}Th) 0.093 (Walter et al., 1997). Both radionuclides are particle-reactive and are removed from the water column by sorption and subsequent burial in the sediments below, a process known as scavenging (Henderson and Anderson, 2003).

Of the two radioisotopes, ^{230}Th has a greater affinity for particles than ^{231}Pa, thus it will be scavenged from the water column much faster than ^{231}Pa. ^{230}Th's partition coefficient, K_d (concentration of ^{230}Th per mass particles divided by ^{230}Th per mass of seawater), is on the order of 10^7 indicating a very particle reactive radionuclide (Henderson and Anderson, 2003). The K_d for ^{231}Pa is an order of magnitude less than ^{230}Th, resulting in a fractionation factor (the ratio of K_d230/K_d231) of ~10, demonstrating the large discrepancy between the scavenging of the radionuclides in the water column (Henderson and Anderson, 2003). Consequently, the residence time of ^{230}Th in the water column is on the order of 10–20 years while the less particle-reactive ^{231}Pa has a residence time of 100–200 years (Walter et al., 1997).

^{231}Pa and ^{230}Th are especially useful in the North Atlantic Ocean, whose waters have a residence time of roughly 100–200 years (McManus et al., 2004). The rapid removal of ^{230}Th prohibits significant lateral transport and causes deposition of ^{230}Th near the site of production, whereas about half of the ^{231}Pa in the water column is "flushed out" of the Atlantic with NADW and is scavenged when it reaches the Southern Ocean (an area of higher particle flux) (Henderson and Anderson, 2003; Yu et al., 1996). Therefore, the sediment record in the North

Atlantic has a ^{231}Pa/^{230}Th ratio lower than that of the production ratio (~0.055), and the Southern Ocean has a ^{231}Pa/^{230}Th ratio higher than the production ratio (~0.150), as a function of the speed of the moving water mass (Marchal et al., 2000; McManus et a., 2004; Henderson, 2002).

Of course this is the modern scenario; since the value of ^{231}Pa/^{230}Th in the sediments depends on the speed of the current, a lower ^{231}Pa/^{230}Th value down-core would imply rapid or intense circulation in the Atlantic, forcing more ^{231}Pa out of the basin before it sorbs and sinks. Conversely, a high ^{231}Pa/^{230}Th value would indicate slower circulation, allowing ^{231}Pa to make its way into the sediment in the Atlantic basin (Henderson and Anderson, 2003).

Influence of Particle Composition

A notable influence on the fractionation of ^{231}Pa and ^{230}Th is the sinking particle flux from the surface. If there is more particulate matter in the water column, more surface area is available for sorption by ^{231}Pa, increasing its rate of deposition to the deep sea sediments and decreasing the fractionation between ^{231}Pa and ^{230}Th (Walter et al., 1997). Ocean margins are a prime example of where this occurs, exhibiting very high rates of particle flux and decreasing the fractionation between particulate ^{231}Pa and ^{230}Th in a process known as boundary scavenging (Yu et al., 1996; Bacon et al., 1988). Boundary scavenging is not as evident in open Atlantic ocean samples relative to the Pacific, mainly due to the short residence time that doesn't allow for sufficient accumulation of ^{231}Pa (Yu et al., 1996).

Therefore, the main concern with the use of ^{231}Pa/^{230}Th in the Atlantic falls to the chemical composition of particles. The potential for particle composition influencing the ratio became increasingly apparent as variability among reported values of fractionation increased with variability in study area, largely due to the opal content of samples (Henderson and Anderson, 2003). In the Southern Ocean, sediment trap and sediment surface data yielded high $^{231}Pa/^{230}Th$ values, paired with relatively low overall particle flux. It was concluded that there must have been a change in chemical composition of the particles that was driving the decreased fractionation of the radionuclides, and it was thought to be the biogenic opal flux (Walter et al., 1997).

Luo and Ku (1999) analyzed samples from sediment traps in the equatorial Pacific and western North Atlantic and found that ^{230}Th is scavenged most efficiently by aluminosilicates (clays/lithogenics) and this component is the primary reason for a fractionation factor of ~10 in the open ocean. Using a two-end-member model, they found that the pure end of non-lithogenics (e.g., carbonate, opal, and organics) was responsible for a fractionation factor of ~1. They ultimately emphasized the importance of opal/clay ratios for ^{230}Th and ^{231}Pa fractionation. These findings were later refuted by Chase et al. (2002) who found that carbonates played a much larger role in scavenging ^{230}Th. Their calculated partition coefficient, "pseudo" K_d, for ^{230}Th actually increased with both lithogenics and carbonate, while decreasing slightly with opal content and not significantly enough to affect overall fractionation. The K_d for ^{231}Pa increased only with increasing opal content and had no significant change for carbonates or lithogenics. The important ratio from this study proved to be opal/carbonate.

Laboratory experiments by Geibert and Usbeck (2004) supported those of Chase et al. (2002) in that their K_d values and fractionation factors were similar in magnitude. They also found ^{230}Th to be efficiently scavenged by each of their particle types (smectite/clay, biogenic opal, manganese dioxide precipitate, and calcite) with slightly higher efficiency in the presence of manganese. Their fractionation factors agreed with Chase et al. as opal fractionated ^{230}Th and

^{231}Pa less than clay. Carbonate, however, proved too variable in their experiments to definitively calculate its fractionation factor.

Roberts et al. (2009) generated data from the Gulf of Mexico and the Sargasso Sea that was comparable to previous studies, and supported the importance of opal and carbonate content on sediment ^{231}Pa/^{230}Th. With the exception of the Luo and Ku data (1999 and 2004), compiled fractionation values for silica were in the range of ≤1 to 2, and carbonate fractionation values were in the range of 40 to 80 (Roberts et al., 2009; Guo et al., 2002; Geibert and Usbeck, 2004; Chase et al., 2002; Anderson et al., 1992). Roberts et al. (2009) also introduced a new possible mode of fractionation through organic content. The addition of extracellular polymeric substances (EPS) in their experiments increased the fractionation of ^{230}Th and ^{231}Pa in both silica and carbonate, suggesting for the first time that carbohydrate-rich EPS increases the K_d (i.e., scavenging) of ^{230}Th. Clearly, there is a need for consideration of particle composition when interpreting sedimentary ratios of ^{231}Pa/^{230}Th as a proxy for paleocirculation.

This thesis will explore the role of biogenic opal on sediment ^{231}Pa/^{230}Th, and will create a history of AMOC, primary productivity, and past surface conditions spanning a portion of the Holocene.

Study Site

This chapter provides background information on the geographic setting of the Bermuda Rise and previous studies that have reconstructed AMOC changes with Bermuda Rise sediments.

Formation and Setting

The Bermuda Rise (Figure 1) is a bathymetric high in the western North Atlantic Ocean roughly 1500 km in length and 500–1000 km across, extending to a height of ~1000 m above the surrounding abyssal seafloor. The average depth of the rise is 4600 m (Vogt and Jung, 2007). The Bermuda Rise is positioned in a southwest to northeast orientation with the Sohm abyssal plain to the northeast, the Hatteras abyssal plain to the west, and the Nares abyssal plain to the south (listed by increasing depth) (Vogt and Jung, 2007). The exact formation of the Bermuda Rise has been debated since it doesn't fit any one model description. One such model is the Morgan-Crough Bermuda plume model that consists of a “lava lamp” effect within the mantle, paired with shifting tectonic plates. However, the rise extends in a direction that is perpendicular to that of plate motion, discounting it. Origins of the rise have been attributed to any combination of the following: uplift by mantle convection, trapped pockets of low-density mantle, thermal expansion, mantle upwelling (Vogt and Jung, 2007).

Located in the subtropical latitudes, the Bermuda Rise lies in the path of Atlantic Meridional Overturning Circulation (AMOC), and more specifically, at the southern and northern extents of North Atlantic Deep Water (NADW) and Antarctic Bottom Water (AABW), respectively. This key location is especially useful for paleocirculation studies as it is extremely sensitive to changes in relative proportions of deep water masses. These changes are then recorded in a variety of paleoceanographic proxies, including paleonutrient levels in the shells of benthic foraminifera. The North Atlantic has also been proven to be more sensitive to changes in $^{231}Pa/^{230}Th$ as a response to changes in AMOC (relative to the entire Atlantic Ocean, or Southern Atlantic basin) (Marchal et al., 2000).

Sediment Characteristics

The Bermuda Rise is a sediment drift site that exhibits an exceptionally high sedimentation rate for a site so far from the continental margin, making it an excellent archive for high resolution studies (Keigwin and Jones, 1989). Sediments at the Rise accumulate at a rate of 10–20 cm/kyr during interglacial periods and 100–200 cm/kyr during glacial periods, allowing for deposits to be quickly covered (Adkins et al., 1997). The Bermuda Rise depends on several modes of sediment transportation because of its isolation from direct continental runoff of sediments. Specifically, fine particles (<63 μm) are released from the Laurentian Fan via turbidity currents, resuspension events on the continental margin release sediments that are trapped in the Western Boundary Undercurrent and deep recirculation gyres, and erosion from the Grand Banks releases sediments to NADW which are then entrained by deep recirculation gyres (Keigwin et al., 1984; McCave, 2002). Course fraction particles (>63 μm), mostly foraminifera, arrive by natural fall-out from the pelagic waters above without significant lateral transport (Keigwin et al., 1984).

Seismic profiles of the northern region of the rise show that sedimentation has been laterally transported since the mid-Eocene (~43 mya) with a series of deposition and erosion events (Ayer and Laine, 1982). More recently, Laine et al. (1994) found that the sediments on the rise experienced a significant erosional event between 63 and 11 kya (Laine et al., 1994).

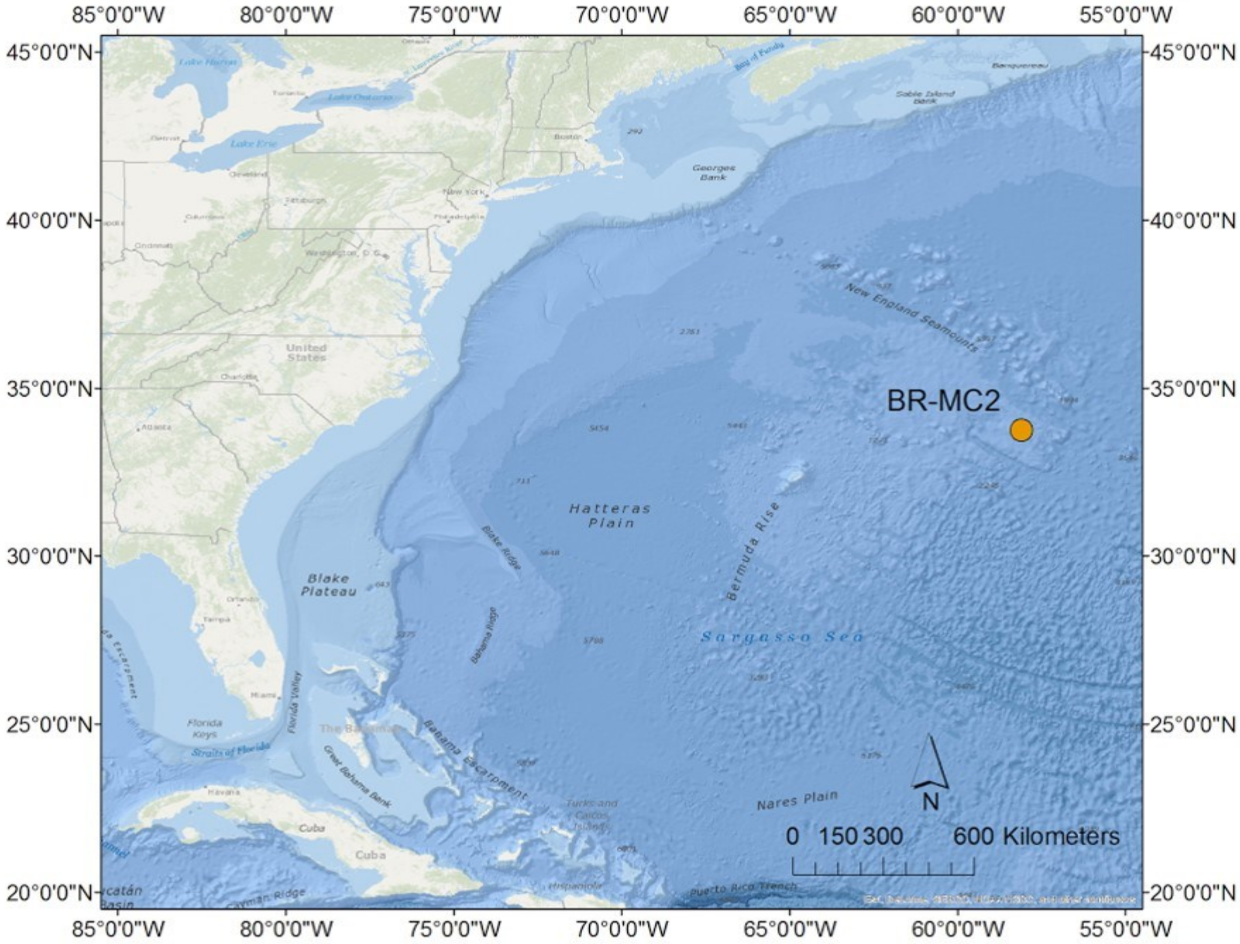

Figure 1. Map of the western North Atlantic Ocean (Sargasso Sea) with location of core BR-MC2 marked by orange dot (33.76° N, 58.11° W, 4580 m depth).

These events can be attributed to benthic storms that increase the energy of the region and can resuspend the sediments below (Laine et al., 1994). The Eastward Scarp (the steep slope at the northeastern portion of the rise) can also undergo events of erosion on the slope as abyssal currents increase in speed up the slope, and deposit these sediments back on the plateau of the rise when they slow (Laine et al., 1994). These events are beyond the timescale of this study, but should be considered for interpretations of earlier data.

Previous Studies

Paleonutrient-Based Reconstructions of AMOC

The relative proportions of NADW and AABW at a given point can be traced through time by examining the $\delta^{13}C$ and Cd/Ca values incorporated into the calcite tests of benthic foraminifera. These proxies have been employed in several studies of past deep water variability and by extension, AMOC, as far back as the interglacial Marine Isotope Stage (MIS) 5 (~131 kya) through the present (Boyle and Keigwin, 1987; Keigwin et al., 1991; Keigwin and Jones, 1994; Adkins et al., 1997).

Boyle and Keigwin (1987) examined sediment from the Bermuda Rise to focus on Atlantic deep water variability in response to the Younger Dryas cooling event to assess the deep ocean response to rapid climate events. The Younger Dryas occurred ~12–10 kya and interrupted a warming trend towards the end of the last deglaciation, returning temperatures in parts of the Northern Hemisphere to near-glacial values for about 1–2 kyr. On the scale of geologic time, this event is considered to be very sudden and few open ocean sites have high enough sedimentation rates to preserve a record of the Younger Dryas (Boyle and Keigwin, 1987). From ~11.5–9 kya, benthic $\delta^{13}C$ values rapidly decreased by a magnitude greater than

1‰ on what was a steady increasing trend toward Holocene values. Similarly, Cd/Ca spiked to higher values on an already decreasing trend, suggesting an increased presence of AABW at the Bermuda Rise and an overall slow-down of AMOC during the Younger Dryas. This study provided the first evidence of a millennial-scale climate event affecting the rate of Atlantic overturning circulation.

Keigwin et al. (1991) looked at the same proxies across the transition of the last deglaciation (~18–10 kya, MIS 2/1) to investigate the role and response of AMOC changes to larger climate events. They found that planktic $\delta^{18}O$ exhibited four distinct peaks during the transition from glacial to interglacial climate: a $\delta^{18}O$ maximum at ~14.5 kya, a minima at ~13.5 and ~12 kya, and another maximum at ~10.5 kya, possibly coincident with the Younger Dryas cooling event. All four events were found to correlate with positive Cd/Ca spikes, suggesting a higher proportion of AABW and less NADW production at these times. Ocean circulation models (Maier-Reimer and Mikolajewicz, 1989; Harvey, 1989; Rind et al., 1986) explained these coupled occurrences as a series of meltwater pulses from different latitudes that affected the temperature and salinity of the surface waters of the Bermuda Rise slightly differently, resulting in opposite $\delta^{18}O$ signals. The minima values are most likely due to meltwater pulse events from the Mississippi River that spread out of the Gulf of Mexico and decreased surface salinity in the subtropical North Atlantic. The freshwater pulses decreased the surface $\delta^{18}O$ signal and stabilized the water column, and reduced the rate of NADW formation (Fairbanks, 1989). The maxima are attributed to meltwater events at higher northern latitudes that injected freshwater directly to the site of NADW formation and immediately halted AMOC, decreasing the surface temperature at the Bermuda Rise from reduced northward surface heat flow, and hence increased $\delta^{18}O$ values (Maier-Reimer and Mikolajewicz, 1989). Keigwin et al. (1991) demonstrated the extreme sensitivity of NADW production to surface salinity variations across the North Atlantic.

Keigwin and Jones (1994) looked further back to investigate the last glaciation (MIS 5/4) ~71 kya. Again using sediments from the Bermuda Rise they found that benthic foraminiferal $\delta^{18}O$ increased steadily across the MIS 5/4 boundary, indicating growth of ice sheets on land. The planktonic $\delta^{18}O$ exhibited a more complicated record with an overall increase in $\delta^{18}O$ indicating cooling surface temperatures and/or an increase in continental ice volume. However, superimposed on this trend were two major oscillations exceeding 1‰ that coincided with spikes in benthic $\delta^{13}C$ and %$CaCO_3$. The benthic $\delta^{13}C$ and %$CaCO_3$ record showed an overall trend of decreasing values interrupted by two major increases that lasted for less than 2 kyr, centered ~72 kya and ~68 kya. This record suggests decreased production of NADW and replacement with AABW interrupted by millennial-scale resumption of NADW circulation. The planktic $\delta^{18}O$ reflected the surface climate response to the changing patterns of circulation, in that pulses of AMOC resumption were accompanied by brief warming surface temperatures. These results paired with Keigwin et al. (1991) suggest that millennial-scale deep water variability during transitions between glacial and interglacial climate is to be expected.

Adkins et al. (1997) used Cd/Ca from Bermuda Rise sediments to study AMOC variability during MIS 5e and 5d (~131–110 kya), the most recent interglacial period that had climate conditions most similar to today. The oldest samples from this study represented the onset of deglaciation ~131 kya, at the transition from MIS 6 (glacial) into MIS 5 (interglacial). In these samples Cd/Ca data indicate low, nutrient-poor deep waters indicating a presence of NADW, then a sudden increase in Cd/Ca sustained for ~1.5 kyr, implying a stronger presence of AABW. Adkins et al. attributed this lessened AMOC to Heinrich events during which large amounts of ice were calved from glaciers and drifted out to the North Atlantic. As these large quantities of ice melted they freshened the surface waters, increasing their buoyancy and reducing the production of NADW. This interpretation was supported by the planktic $\delta^{18}O$ signal that decreased sharply at the same time, indicating warming and decreasing surface salinity. By ~129 kya (the start of MIS 5e), Cd/Ca values decreased again indicating a resumption of NADW production, and remained relatively steady until ~118 kya, the transition from full interglacial climate of 5e into the relatively cooler 5d. At this time Cd/Ca values indicated a rapid increase in AABW presence as they spiked to unusually high values in the span of ~400 yr. The interglacial trends exhibited a relatively stable climate similar to that of the present Holocene, but the transition suggests that large climate shifts can cause deep-waters to react rapidly and even act as a positive feedback, cooling the higher northern latitudes further as AMOC slows (Adkins et al., 1997).

Paleonutrient-based studies in the North Atlantic have provided valuable insight into past changes in AMOC. Through the works discussed here, it is clear that AMOC is capable of reacting to rapid climate forcing, and has the potential to change significantly in the span of several hundred years. It was also evident that these proxies are subject to multiple and occasionally conflicting interpretations. An additional complication of paleonutrient proxies is that they can also be "reset" by the calcite saturation of bottom waters, air-sea interactions, or any number of biological processes (Lynch-Stieglitz et al., 2007).

$^{231}Pa/^{230}Th$-Based Reconstruction of AMOC

To investigate the changes in flow rate of AMOC in response to climate forcing, $^{231}Pa/^{230}Th$ data has been collected across the North Atlantic basin (Yu et al., 1996; Gherardi et al., 2005; Guihou et al., 2010) while values produced from the Bermuda Rise include McManus et al. (2004) and Lippold et al. (2009).

Yu et al. (1996) examined the Last Glacial Maximum (LGM; ~17.5–19.8 kya) to resolve conflicting models of AMOC based on benthic $\delta^{13}C$ and Cd/Ca data across the Atlantic. Nutrient data from the Atlantic and Southern Oceans provided three different possible explanations for past circulation changes during the LGM: first, Atlantic intermediate water shoaled and ceased to produce deep water masses all together; second, intermediate water circulation was strong enough to circulate directly to the Indo-Pacific Ocean and did not reach the Southern Ocean at depth; third, intermediate water shoaled, but remained strong enough to produce deep water and AMOC rates were similar to that of today.

To provide additional data and clarify which mode of AMOC was correct, Yu et al. compiled $^{231}Pa/^{230}Th$ data from sites from both the North and South Atlantic and averaged the export of the radioisotopes to the Southern Ocean during the Holocene and the LGM. They determined that during the LGM overturning circulation was similar to that of today but there was enhanced production of intermediate waters known as Glacial North Atlantic Intermediate Water (GNAIW). These results favored the third proposed model above, and support the results of the benthic Cd/Ca data previously noted. Yu et al. illustrated complications to nutrient-based proxies and the need for several independent circulation proxies when interpreting AMOC changes, and were the first to implement the use of $^{231}Pa/^{230}Th$ ratios as a paleocirculation proxy.

McManus et al. (2004) looked at paleocirculation changes from the LGM to the present and found two major events in which AMOC was rapidly reduced: one associated with Heinrich Event 1 (H1) followed by rapid warming, and the second coinciding with the Younger Dryas also followed by abrupt warming. They found the mean $^{231}Pa/^{230}Th$ ratio for the LGM to be 0.068 (±0.010), indicating slightly slower overturning relative to mean Holocene values (0.055 ±

0.006). As the deglaciation began, the ratio of $^{231}Pa/^{230}Th$ jumped from values around .068 to just below the production ratio around 0.090 in a time span of less than 1 kyr, indicating an incredibly fast near-complete shut-down of AMOC. McManus et al. found that the shut-down coincided with the H1 event and was accompanied by increased planktic foraminiferal $\delta^{18}O$ values, implying cooling of the region without heat being transported via AMOC. At ~14.7 kya AMOC recovered more rapidly than it had ceased, and $^{231}Pa/^{230}Th$ values dropped to around 0.065 in the timespan of ~500 years. This resumption was just before the beginning of the Bølling-Allerød warm period (~14.5–13 kya), suggesting the return of heat transport as AMOC was rejuvenated.

These reduced $^{231}Pa/^{230}Th$ values only held for ~1.5 kyr, as they increased rapidly again to ~0.075 around 12.7 kya. This change in circulation is coincident with the Younger Dryas and another $\delta^{18}O$ cooling signal. McManus et al. also found ice rafted debris in the core during this time, suggesting another iceberg calving event could be the cause of this occurrence of weakened AMOC. The recovery after the Younger Dryas was more gradual than the H1 recovery in that it took ~2.7 kyr for $^{231}Pa/^{230}Th$ values to fall to modern/Holocene values, ~0.055, which was maintained through the present. The results of McManus et al. generally agree with those previously described of Keigwin et al. (1991) and Yu et al. (1996), and support the important role that salinity-driven buoyancy plays in AMOC, as well as the abrupt rate at which it can respond to any changes.

Guihou et al. (2010) obtained sedimentary $^{231}Pa/^{230}Th$ from the eastern and western North Atlantic that spanned the last glacial inception/MIS 5 (~127–60 kya). They found that AMOC during MIS 5e was similar to that of today, and gradually slowed into MIS 4. Overlain on this trend were three major oscillations that only lasted a few thousand years occurring at the transition from 5d to 5c, during 5b, and at the transition from 5a to 4. To uncover the forcing mechanisms of these variations, Guihou et al. compared the radionuclide record to that of Northern Hemisphere summer insolation and found that the oscillations in AMOC occurred after peaks in insolation, lagged by several thousand years. The first oscillation was 18 kyr after a peak, the second lagged by 11 kyr, and the third had no lag at all. They suggested that the decrease in the response time of AMOC occurred as the size of continental ice sheets increased, supporting an indirect link between not only AMOC and ice sheet dynamics, but also Northern Hemisphere summer insolation.

Our understanding of AMOC variability has greatly improved through the use of $^{231}Pa/^{230}Th$, but it is also clear that additional work needs to be done with regards to particle influence on the proxy and additional records from other locations. There are discrepancies between identical cores processed by different groups (McManus et al., 2004 and Lippold et al., 2009) and the same relationship between opal flux and $^{231}Pa/^{230}Th$ does not always hold true for different locations in the North Atlantic basin at varying depths. It is the goal of this study to contribute towards our understanding of past circulation variability, as well as the limitations and potential influences on the sediment $^{231}Pa/^{230}Th$ record at the Bermuda Rise.

Materials and Methods

This chapter presents how the materials used for my study were collected, where they came from, and the analytical techniques that were applied to generate my data.

Sediment Sampling

In August 2012, as part of the Bermuda Rise Particle Flux (BaRFlux) project, a multicore was taken at the Bermuda Rise (33.76º N, 58.11º W at a depth of 4580 m) aboard the *R/V Endeavor*, cruise 513. One of the subcores from that multicore, BR-MC2, was used for this study as it collected the most sediment (47.5 cm) while maintaining an undisturbed sediment-water interface. On board, the seawater from the top of the core was siphoned off to prevent core-top disturbance. The core was then capped and sealed at both ends and remained refrigerated for transit back to the lab.

Subsamples of BR-MC2 were taken at 0.5 cm intervals using a core extruder. The bottom cap was replaced by a plug that was pressed up into the core at set increments, and the 0.5 cm of sediment being displaced at the top was transferred to a sample bag using a clean spatula. Each of the 95 samples were freeze-dried for later processing.

Biogenic Opal Analysis

Approximately 50 mg of dry sediment was taken from each sample (in batches of 20 samples per run) and processed following the procedures outlined by Mortlock and Froelich (1989). This specific method involved hydrogen peroxide and hydrochloric acid rinses to remove any contaminants on the silica and eliminate any organics or carbonates. A 2 M Na_2CO_3

leach was then used to dissolve the silica which was quantified through molybdate-blue spectrophotometry and converted to %Opal (Mortlock and Froelich, 1989). Ten samples throughout the core were run as duplicates to ensure reproducibility. Using the dry bulk sediment masses of each sample, mass accumulation rates of opal were calculated. Opal mass accumulation rates were driven by a shift in the overall sedimentation rate (Figure 3, B), so %Opal was converted to opal flux using a 230-thorium normalization method after Suman and Bacon (1989) to be discussed later in this chapter.

Replicate analyses of standards yielded an average analytical precision (1σ) of ± 0.0037 mM (~2% of the measured value, not overall %Opal) during the period of data generation for this study. Replicate analyses on approximately 10% of the total samples yielded an average standard deviation (1σ) of ± 0.377 %Opal.

Stable Isotope Analyses

Approximately 3 g of each freeze-dried sample was transferred to a 250 mL beaker and saturated with deionized water. This mixture was poured into a 63 μm sieve and rinsed with deionized water until all of the mud had passed through the sieve, collecting in a jar below. The clean sample remaining in the sieve, > 63 μm, was transferred back to the beaker and dried in an oven at 55º C. The < 63 μm fraction in the jar was poured into a 1000 mL beaker and left to settle out. Once settled, the water was poured off and the fine-fraction sample was left to evaporate to dryness, then stored in glass vials.

After being completely dried, the > 63 μm fraction was dry-sieved with a 150 μm sieve and the >150 μm fraction was used to pick foraminifera for stable isotope data while the 63 μm–150 μm fraction was stored in glass vials. The species chosen for the stable isotope analyses was

Globigerinoides ruber (white variety). This species of foraminifera is ideal because it lives at the surface year-round and maintains a consistent annual flux to the sea floor (Keigwin, 1996). The > 150 µm fraction was poured onto a gridded metal tray and examined under a dissecting microscope. White *G. ruber* were individually picked from the tray until ~60 µg of calcite was collected (~12 individuals) per sample. The foraminifera were placed in a 4-hole slide and secured with a glass cover, packaged and transported to the University of South Carolina where they were run on a VG Optima Stable Isotope Ratio Mass Spectrometer (SIRMS) for both carbon and oxygen stable isotope analysis. Samples were reacted at 90°C in phosphoric acid, and all isotope data are reported relative to Vienna Pee Dee belemnite (VPDB) via our working standard, NBS-19. Replicate analyses of this standard yielded an analytical precision (1σ) of ± 0.08‰ for $\delta^{18}O$ and ± 0.06‰ for $\delta^{13}C$ during the period of data generation for this study.

Age Model

Sediments from BR-MC2 were dated using accelerator mass spectrometry ^{14}C. Radiocarbon dating required 5–10 mg of carbonate material per sample, much more material than was obtained from washing sediment for stable isotope analyses. Specific sample depths were chosen for dating, and approximately one-third by weight of the remaining freeze-dried samples was washed and separated into size fractions following the same procedures as the stable isotope analyses. Sample depths were 0.0–0.5 cm (core top), 11.0–11.5 cm, 23.0–23.5 cm, 35.0–35.5 cm, and 47.0–47.5 cm (core bottom). There were not enough *Globigerinoides ruber* in each sample to provide the necessary mass, so a mixture of planktonic foraminifera was selected; species included *Globigerinoides ruber* (white and pink varieties), *Globigerina bulloides*, *Globigerinoides sacculife*r, and *Orbulina universa*.

After approximately 7 mg of carbonate was picked per sample, the foraminifera were cleaned to remove any impurities that could alter the ^{14}C measurements. Each set of foraminifera was transferred to a 50 mL beaker and 20 mL of deionized water was added. The beakers were sonicated for one minute and water was then pipetted out of the beaker to reduce the volume as much as possible without removing any foraminifera. Once the volume was reduced, 20 mL of methanol was added to the beaker and sonicated again for one minute. The methanol was then pipetted out and the beakers were placed in an oven at 55º C for several hours to dry. Once dried, the samples were stored in glass vials and packaged for transport to the University of California, Irvine, and analyzed at the W.M. Keck Carbon Cycle Accelerator Mass Spectrometer (KCCAMS).

The resulting ^{14}C ages were calibrated using the CALIB 7.0 radiocarbon calibration program which used a correction of -125 years to account for the difference between the global average reservoir age and the Bermuda Rise. The core-top contained excess ^{14}C, resulting in a negative radiocarbon age of -555 years. This was the result of modern nuclear weapons testing so this sample was set to 0 years before present. After calibration to calendar years before present (ybp), it was evident that this sediment core resolved almost the entirety of the most recent interglacial epoch, the Holocene (~10 kya–present) (Table 1).

Linear interpolation between ^{14}C-dated depths provided an age model that was applied to all other datasets obtained in this study. Based on this age model, sedimentation rates through the early Holocene were calculated to be ~3.9 cm/kyr, then increased to ~8.6 cm/kyr at 2740 ybp (Figure 2). These estimated linear accumulation rates were then converted to mass accumulation rates using the dry bulk densities and ^{14}C ages of each sample (Appendix I). The mass accumulation rates, however, do not account for variability within each dated interval and shift

Depth Interval (cm)	Raw AMS ^{14}C Age (Years BP)	Error	Calibrated Calendar Age (Years BP)	Error (2σ)
0.0–0.5	-555	15	0	0
11.0–11.5	1660	15	1326.5	47.5
23.0–23.5	2840	15	2740	39
35.0–35.5	5470	20	5988	82
47.0–47.5	8255	25	8974.5	94.5

Table 1. Radiocarbon dated samples with their respective raw ^{14}C ages and calibrated years before present.

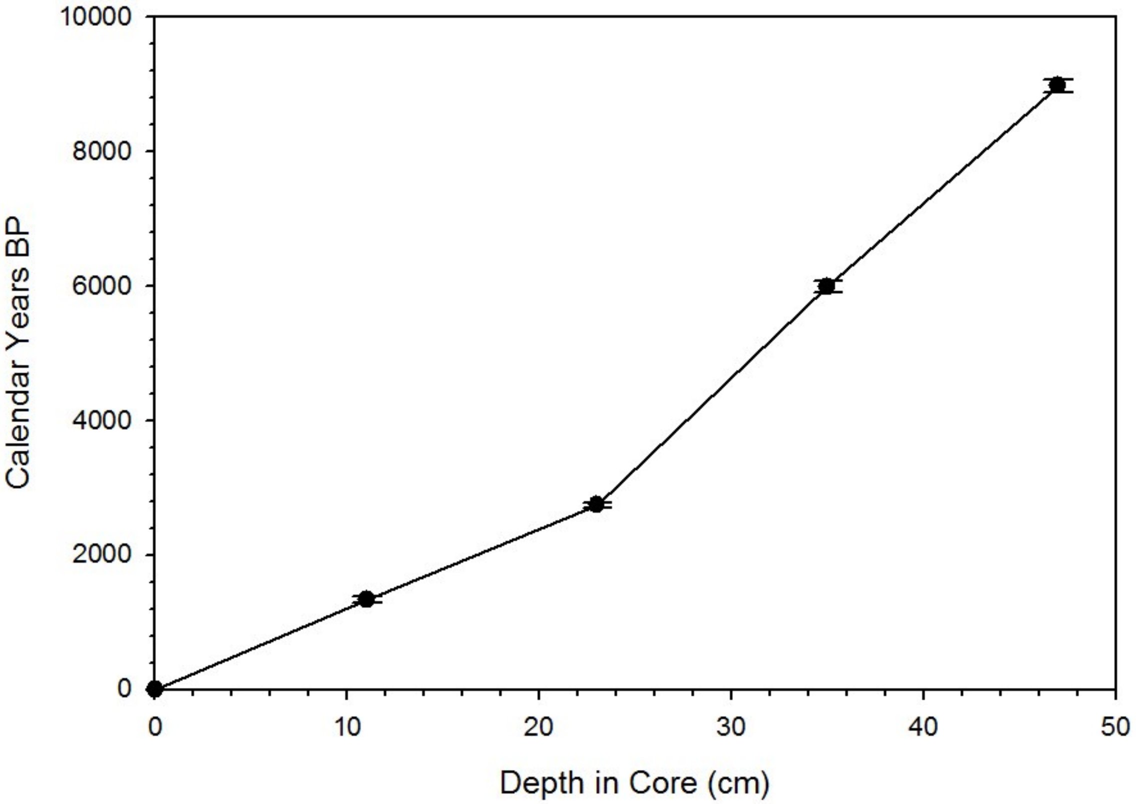

Figure 2. Age versus depth based on calibrated ^{14}C ages with error bars indicating 2σ. Linear interpolation between points determined the age model used in this study.

slightly with each change in the interpolated sedimentation rates. To adjust for this, sediment flux was also calculated using a 230-thorium normalization method after Suman and Bacon (1989), calculations described later in this chapter.

It must be noted that excess ^{210}Pb was measured in the surface sediments of a different subcore (BR-MC1) from the same multicore deployment. With a short half-life of ~22 years, the presence of ^{210}Pb several centimeters into the core indicates a homogenized mixed layer due to bioturbation (Nozaki et al., 1977). This implies that the top 10 cm (or most recent ~1 kyr in the age model) are actually mixed and any samples in this portion of the sediment record should be interpreted as having a uniform age.

Radionuclide Analysis

All acids used in this study were trace metal grade and the water was 18 MΩ Milli-Q. Approximately 1–2 mL of water was added to 100 mg of freeze-dried sediment, and the samples were spiked with ^{229}Th, ^{233}Pa, and ^{236}U to determine recovery for those elements. Ten mL of concentrated (16 N) HNO_3 and 1 mL HF were then added to each sample and after carbonate degassing was complete, the samples were digested in a Milestone Ethos EZ microwave digestion system for 25 minutes at 180°C. After digestion, there were no visible particles in the microwave vessels. The samples were then transferred to 50 mL centrifuge tubes and spun for 10 minutes, after which a small amount of white precipitate became visible. The supernatant was pipetted into 50 mL Teflon (PTFE) tubes and the remaining precipitate was measured on a gamma counter to make sure that no significant amount of ^{233}Pa was sorbed to it.

The Teflon tubes were set in a SCP Science DigiPREP Jr digestion block and 0.2 mL $HClO_4$ was added to the samples before being heated, uncovered, at 120°C. The perchloric acid prevented the sample from drying out completely while the volume was reduced to 0.5 mL. The walls of the tubes were periodically rinsed with 8 N HNO_3 to be sure that all of the sample remained at the bottom. Once the volume was reduced to slightly less than 0.5 mL, 3–5 mL of 8 N HNO_3 was added and the volume was reduced again. Two mL 8 N HNO_3 was then added and each sample was pipetted to 15 mL centrifuge tubes. The Teflon tube was rinsed with 8 N HNO_3 and the rinse was also transferred to the centrifuge tube.

The samples were then spiked with 0.15 mL $FeCl_3$ (150 mg/mL)/ 5% HCl mixture and vortexed. The iron mixture attracts the Th, Pa, and U while any fluorides are left to be discarded. NH_4OH was then added slowly until iron precipitates formed and settled out of solution (~4 mL per sample was used). The samples were centrifuged for 10 minutes and the supernatant was pipetted off and discarded. The precipitate was then washed twice by adding 5 mL water, vortexing and centrifuging, then discarding the supernatant. After dissolving each sample in 2 mL 8 N HNO_3 and vortexing, samples were transferred back to the Teflon tubes, the centrifuge tubes were rinsed with 8 N HNO_3, and that was transferred as well. The volume of each sample needed to be reduced again, so 0.2 mL $HClO_4$ was added and the same procedures were followed as the previous volume reduction. After the nitric acid addition and volume reduction to less than 0.5 mL, the samples were ready for separation.

Plastic chromatography columns (Bio-Rad Poly-Prep, 10 mL) were loaded with 3 mL Bio-Rad AG 1-X8 Resin (100–200 mesh) which were then conditioned by filling the columns once with water (drained to waste), followed by a full volume of ~12 N HCl (also drained to waste), and this rinsing process was repeated twice. The samples were then dissolved in 1 mL concentrated HCl and 15 mL Teflon (PFA) vials were placed under each column to catch the Th fractions. Each sample was then pipetted onto its corresponding column, and the Teflon tubes were rinsed with 1 mL concentrated HCL which was also loaded on the column. The Th fraction was eluted immediately, and the columns were filled with concentrated HCl to be sure all of the Th drained to the vials below. The Th vials were replaced with new 15 mL Teflon vials and Pa was eluted with a mixture of concentrated HCl and 0.2 N HF. After replacing the vials again, water was used to elute U (it created a dilute HCl mixture with the residual HCl in the resin). The Th and U splits were evaporated to dryness on a hotplate within an air filtration system at 115°C, while the Pa split was evaporated down to a low volume (< 0.5 mL) for later purification.

One mL 8 N HNO_3 was added to the Th and U fractions, and 1 mL concentrated HCl was added to the Pa fraction, and all were evaporated down to their respective volumes again. Columns were loaded with 2 mL of new resin for purifying the Th split. The resin was conditioned following the same rinsing procedures above, but with water and 8 N HNO_3. The Th samples were dissolved in 1 mL 8 N HNO_3 and loaded onto the column (a rinse of the vial with 1 mL 8 N HNO_3 followed and was also loaded onto the resin). The columns were flushed once with 8 N HNO_3 to remove any impurities, and Th was eluted again with a full-column rinse of ~12 N HCl into a Teflon vial below. The vial of Th sample was then evaporated to dryness.

Pa was purified by conditioning 2 mL of new resin as before with water and ~12 N HCl. Pa samples were dissolved in 1 mL ~12 N HCl and loaded onto their corresponding columns (the vials were also rinsed and loaded) and a flush of HCl followed to clean the samples. Pa was eluted with the HCl/dilute HF mixture into a Teflon vial below. These samples were evaporated down to less than 0.5 mL.

Since some iron was visible in the U samples, the U was purified with new resin conditioned three times with water and 8 N HNO_3 rather than HCl. The U samples were dissolved in 1 mL 8 N HNO_3 and loaded onto the columns. The Teflon vials were also rinsed with 8 N HNO_3 and loaded onto the columns. The columns were then rinsed with one volume full of 8 N HNO_3 to rinse the samples and the U was eluted with 0.1 N HCl into the Teflon vials below. These samples were evaporated to dryness.

After the samples evaporated to their desired volumes, each was dissolved in 1 mL of a 2% HNO_3/dilute HF mixture and transferred to a 2 mL centrifuge tube (the vial was rinsed with 0.5 mL of the same mixture and transferred to the tube). The samples were then spun for 5 minutes to remove any residual particles and pipetted into new 2 mL centrifuge tubes (leaving behind one drop of solution) to be run on a Nu Plasma II Multi-Collector Inductively Coupled Plasma Mass Spectrometer (MC-ICPMS) available at the Facility for Isotope Research and Student Training (FIRST) at Stony Brook University.

The activities of parent uranium isotopes (234 and 235) were calculated based on the amount of ^{238}U relative to the ^{236}U spike. After ^{238}U was corrected for any ^{236}U contamination, the production of ^{234}U and ^{238}U were assumed to be in equilibrium, and ^{235}U was calculated using the known natural crustal abundance of $^{238}U/^{235}U$ atoms (7.25×10^{-3}). Although not entirely necessary because of their long half-lives, ^{234}U and ^{235}U (half-lives of ~2.5×10^{5} and ~7.0×10^{8}, respectively) were then corrected for decay since time of deposition using the equation:

$$A_0 = A_f / e^{(-\lambda t)}, \tag{1}$$

where A_f is the calculated activity of the isotope (dpm/g), λ is the decay constant (years^{-1}), and t is the age of the sample (years) (Cheng et al., 2000; Jaffey et al., 1971).

The activity of ^{230}Th was then calculated based on the relative abundance of the ^{229}Th spike. The activity of its parent isotope, ^{234}U, was then subtracted to determine excess ^{230}Th ($^{230}Th_{xs}$). $^{230}Th_{xs}$ was also corrected for decay since deposition using equation (1). In general, the same procedures were followed for the determination of excess ^{231}Pa (^{231}Pa$_{xs}$) relative to its parent ^{235}U. The measured ^{231}Pa was also corrected for the percent recovery, using a seawater standard, before being adjusted for in situ production and decay. Some amount of ^{237}Np remains in the ^{233}Pa spike (from spike production), and the seawater standard allows for the correction of ingrowth of ^{233}Pa during sample processing since we know the value that should be measured. Unfortunately, the standard was seawater and not sediment, and this created difficulties while processing the samples. Analysis of the standard yielded 196% recovery of ^{231}Pa in the first set of Pa samples (batch 3), then 1277% recovery in the second set (batch 4). Applying this enormous correction to the ^{231}Pa data in this batch produced values that were well beyond the rest of the dataset. Therefore, the correction of the 196% yield was applied to batch 3, and there was no seawater standard correction applied to the batch 4.

Samples were taken from 5 depths evenly spaced throughout the core and were analyzed several times for replicate analyses. Five depths within the top ~11 cm (~1266 ybp) were also run to fill in more modern changes (see Appendix II for full list of samples). Average ^{230}Th$_{xs}$ and ^{231}Pa$_{xs}$ values were used in the determination of ^{231}Pa$_{xs}$/^{230}Th$_{xs}$. Due to the lack of desired sampling resolution from BR-MC2, additional ^{231}Pa$_{xs}$ and ^{230}Th$_{xs}$ data were compiled from cores KNR31 GPC5 (33° 41.2’ N, 57° 36.9’ W, 4583 m) and OCE326 GGC5 (33° 42’ N, 57° 35’ W, 4550 m) (Suman and Bacon, 1989; McManus et al., 2004) excluding the top 4 cm of each core to account for the homogenized, mixed layer.

Thorium samples were consistently well measured on the MC-ICPMS, so the sample with the most ^{230}Th$_{xs}$ replicates (free from surface sampling error) provided a lower boundary error of 1% for the analysis (standard deviation of the samples over the average ^{230}Th$_{xs}$). Protactinium samples were not as consistent, so the surface ^{231}Pa$_{xs}$ replicates provided an upper boundary error of 34% (standard deviation of the sample results over the average $^{231}Pa_{xs}$).

$^{230}Th_{xs}$ Normalization

There are a few major complications that accompany the use of mass accumulation rates to determine sediment flux: the assumption of a linear accumulation of sediments between dated horizons, and the overestimation of true vertical flux which cannot be distinguished from sediments advected by bottom currents (Francois et al., 2004). Bacon (1984) found that the use of $^{230}Th_{xs}$ normalization can resolve these problems as ^{230}Th has a nearly constant flux to the seafloor that is equivalent to its known production in the overlying waters:

$$Flux_{230} = Production_{230} = \beta_{230}, \tag{2}$$

where production is based on water depth, z (meters):

$$\beta\ (dpm/cm^2/kyr) = 0.00263z \tag{3}$$

It follows that the flux of any sediment constituent can be calculated by multiplying its weight fraction by the production rate of ^{230}Th and normalizing that to the excess, decay corrected ^{230}Th in that sample:

$$R_i = \beta f_i / {}^{230}Th_{xs}, \tag{4}$$

where f_i is the weight fraction of the constituent (Suman and Bacon, 1989).

This calculation was applied to the overall sediment flux (Figure 3, A) and biogenic opal flux (Figure 3, B) in this study to correct for variations in sediment flux caused by possible resuspension events by bottom currents.

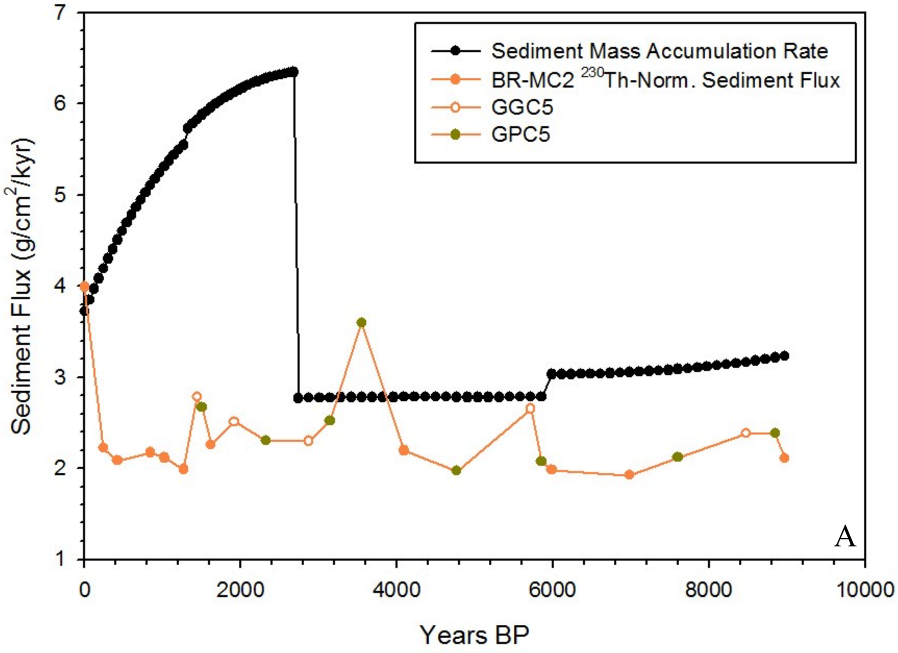

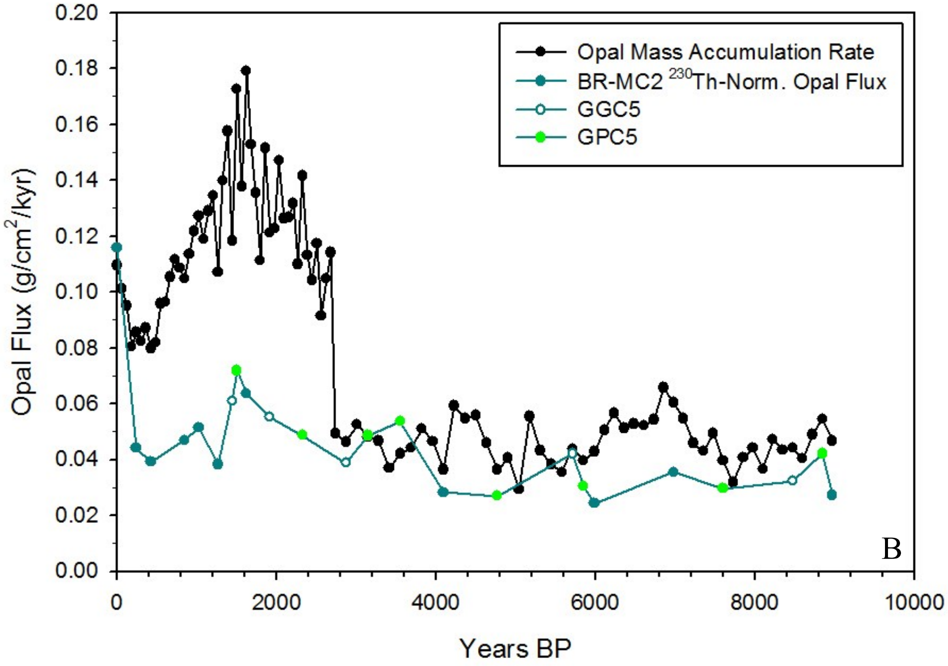

Figure 3. (A) Comparison of total sediment mass accumulation rate and $^{230}Th_{xs}$-normalized sediment flux. The mass accumulation rate is consistently an overestimation of the true sediment flux driven by shifts in the age model, and the $^{230}Th_{xs}$-normalized flux produces a clearer record of sediment flux variability. The mass accumulation rates can thus be interpreted as changes in sediment focusing at the Bermuda Rise (Francois et al., 2004). (B) Comparison of biogenic opal mass accumulation rate and $^{230}Th_{xs}$-normalized opal flux. This record also demonstrates the need for $^{230}Th_{xs}$ normalization.

Results

This chapter presents the results from the analyses of sediments collected in BR-MC2. Raw data for each variable (e.g., stable isotope data, percent opal data, etc.) can be found in the Appendices at the end of this thesis.

Sedimentation Rates

Based on the age model for the core used in this study, the Bermuda Rise has maintained an average sediment flux of 2.4 g/cm^2/kyr throughout the Holocene. However, during this time there have been several pulses of slightly increased flux that have lasted no more than 1 kyr, and none have exceeded a 2 g/cm^2/kyr increase. A record of the $^{230}Th_{xs}$ normalized sediment flux can be seen in Figure 4 and includes $^{230}Th_{xs}$ values from cores GPCG and GGC5 (Suman and Bacon, 1989 and McManus et al., 2004). The early Holocene is characterized by the lowest amount of sediment flux and remains within the range of 1.9–2.4 g/cm^2/kyr from 8974 to 5852 ybp, after which there is a small maximum of 2.7 g/cm^2/kyr at 5717 ybp. By 4770 ybp the sediment flux returned to 2.0 g/cm^2/kyr and was consistent until a larger pulse to 3.6 g/cm^2/kyr at 3552 ybp. This event was shorter lived and the sediment flux returned to 2.3 g/cm^2/kyr by 2875 ybp. The sediment flux slowly climbed to 2.8 g/cm^2/kyr by 1444 then dropped off to 2.0 g/cm2/kyr in less than 200 yr. Values remained near this minimum until the largest pulse of sediment at the present to 4.0 g/cm^2/kyr.

Stable Oxygen Isotopes

The planktonic foraminiferal $\delta^{18}O$ record (*G. ruber*) is shown in Figure 5. Note that the

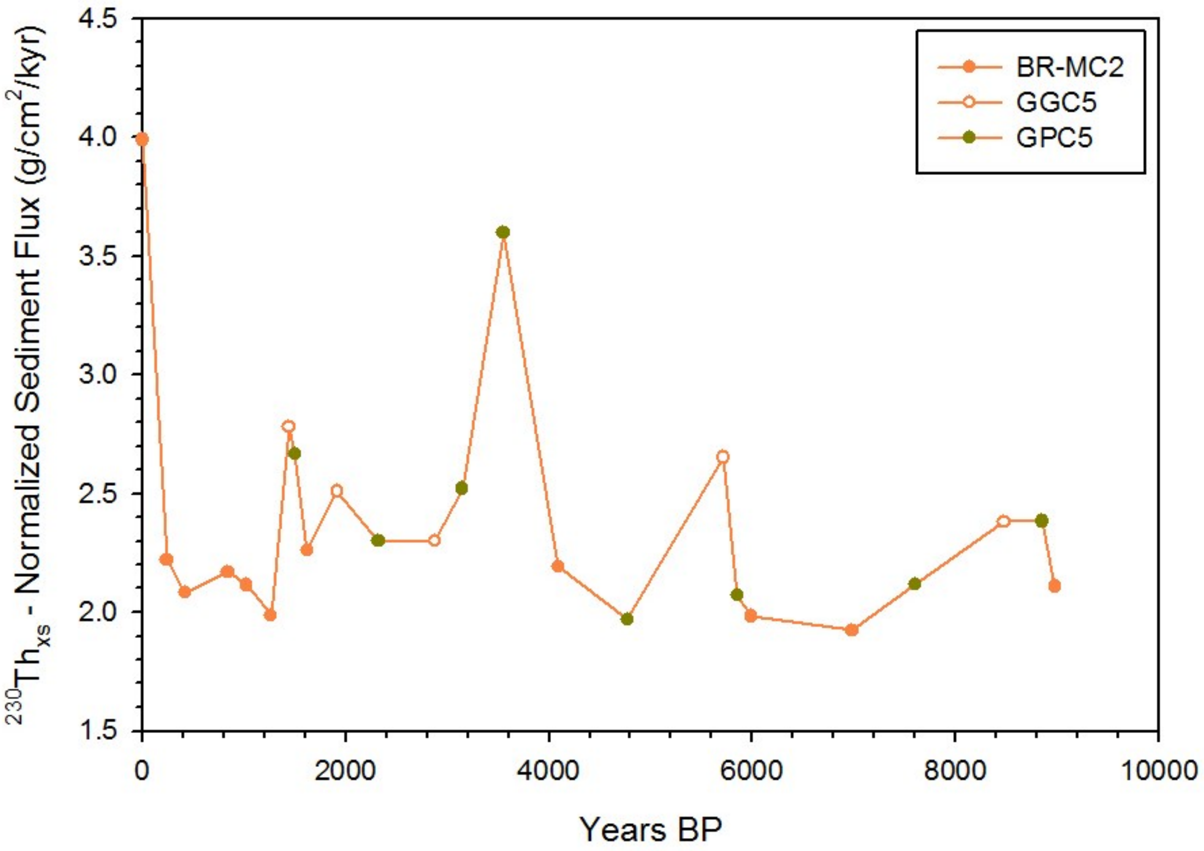

Figure 4. ^{230}Th normalized overall sediment flux using sedimentary $^{230}Th_{xs}$ values from BR-MC2, GGC5, and GPC5.

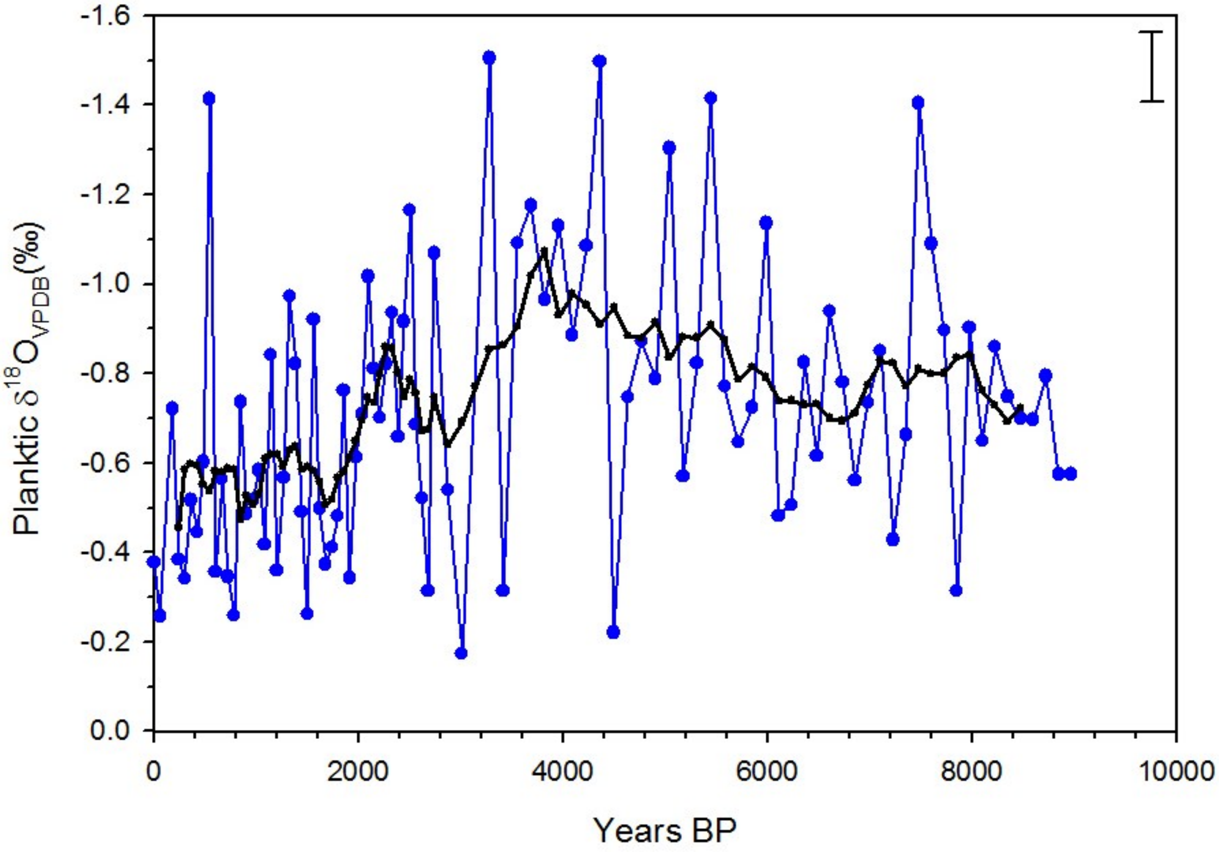

Figure 5. Planktic stable oxygen isotope record for BR-MC2 with 9-point running average overlain. Note the inverted y-axis to illustrate changes in temperature (less negative values indicate cooling, while more negative values indicate warming). Error bar in the top right corner notes the ± 0.08‰ (1σ) error associated with the analytical precision of the standard.

y-axis is inverted to illustrate the inverse relationship between $\delta^{18}O$ and sea surface temperature. The 9-point running average has also been overlain on the plot to increase the clarity of trends in the oxygen isotope record.

The data display a trend of overall isotopically lighter values for the early half of the sediment record that become lighter from ~9000–3800 ybp, then heavier towards the present. Superimposed on this trend are local maxima and minima. The earliest samples (~9000 ybp) exhibit $\delta^{18}O$ values near -0.70‰, then become lighter to reach a local minimum near -0.80‰ that is sustained for roughly 800 yr. Average values then return to ~ -0.70‰ at 6800 ybp, just before a steady trend of increasingly lighter values from 6800–3800 ybp. The average $\delta^{18}O$ then reaches ~ -1.1‰ which is the lightest value of the record, and a turning point where $\delta^{18}O$ values become heavier towards the present. During this time (~3800–0 ybp), there is an interval from ~2800–2300 ybp where average values briefly become lighter, jumping from -0.64‰ to -0.86‰ then returning to -0.52‰ by ~1700 ybp. There is another light interval from ~1700–1000 ybp where $\delta^{18}O$ values reach -0.60‰. They become slightly heavier by ~900 ybp (-0.47‰) before a third lighter interval beginning at ~700 ybp (-0.58‰). From ~300 ybp to the present, average values decrease again toward -0.40‰.

Stable Carbon Isotopes

The planktonic $\delta^{13}C$ record from *G. ruber* is shown in Figure 6. This stable isotope record has also been overlain with a 9-point running average to increase the clarity of trends. The data show overall steady $\delta^{13}C$ values for the early half of the record (~9000–4200 ybp), maintaining average values around -0.35‰. Interrupting this steady trend is a small maximum from ~7400–6100 ybp where values become heavier, increasing from -0.49‰ to -0.18‰ before

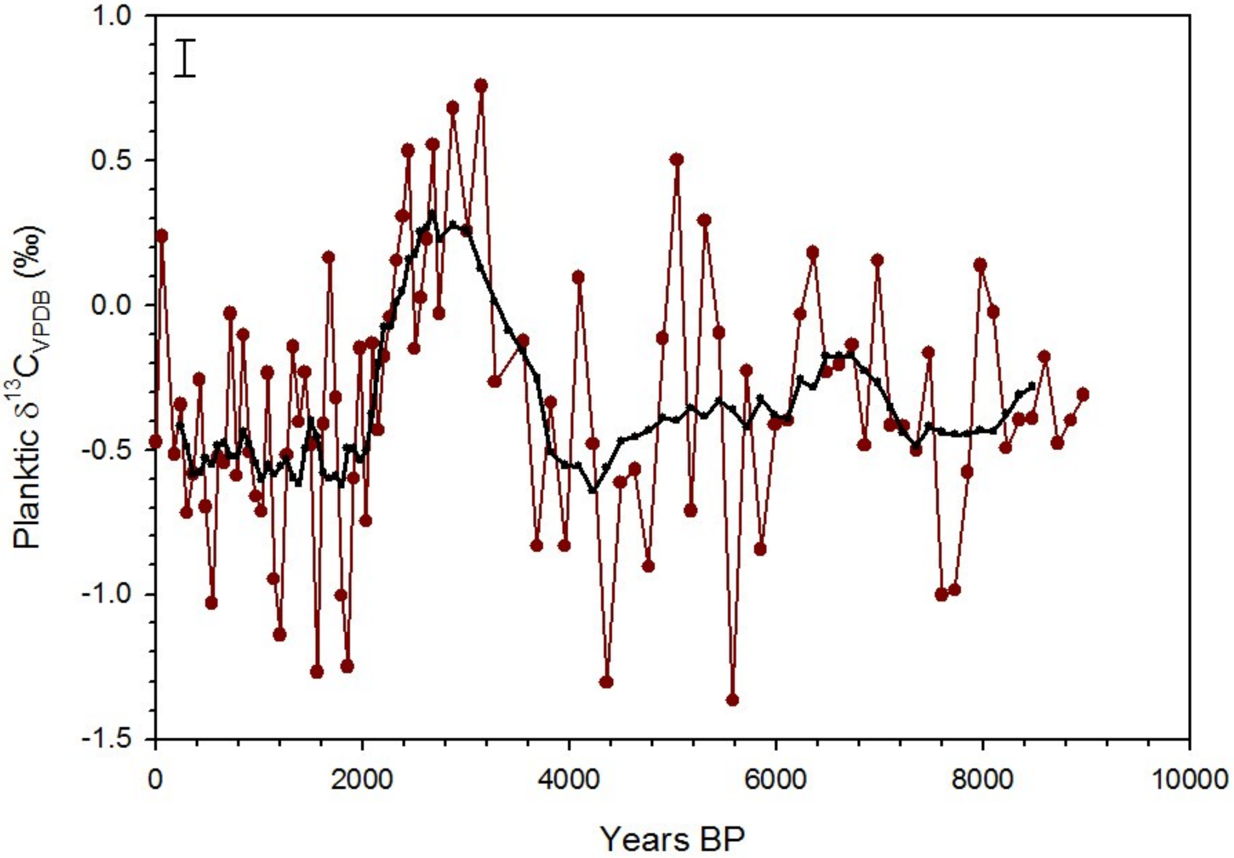

Figure 6. Planktic stable carbon isotope record for BR-MC2 with 9-point running average overlain. Error bar in the top left corner notes the ± 0.06‰ (1σ) error associated with the analytical precision of the standard.

returning to -0.39‰. Average values then begin a slight decreasing trend to ~4200 ybp where values reach -0.66‰ before a ~2000 yr interval of isotopically heavier values. At ~4200 ybp $\delta^{13}C$ values climb to 0.32‰ by ~2700 ybp, but aren't maintained for a long period of time, as they begin a rapid decline to lighter values near -0.62‰ by ~1800 ybp. From this point towards the present, $\delta^{13}C$ values remain within the range of -0.62‰ to -0.41‰ with small oscillations.

Biogenic Opal Flux

Biogenic opal appears to be a very minor component of sediments at the Bermuda Rise. This study found that the %Opal in each sample remained within the range of 1.1–2.9% (Figure 7, A). Opal content remained lower during the early Holocene with values near 1.3% that increased to an average of 1.8% from ~7100–6100 ybp. A decrease down to near 1.5% followed at ~6000 ybp. After this, there was a steady increase to a maximum of 2.8% at ~1600 ybp. The %Opal then steadily decreased to 1.9% until ~400 ybp where values then increased rapidly to the modern value of 2.9%. For reasons discussed in the previous section, the $^{230}Th_{xs}$ normalized opal flux will be used throughout the remainder of this thesis.

The $^{230}Th_{xs}$ normalized opal flux (henceforth referred to as "opal flux") remained within the range of 0.027–0.116 g/cm^2/kyr (Figure 7, B). The overall trend of the opal flux record consists of increasing values (from 0.027 g/cm^2/kyr to 0.044 g/cm^2/kyr), from ~9000 until 200 ybp when there is a factor-of-three increase to the core top to 0.116 g/cm^2/kyr. There are several small peaks superimposed on the opal flux record in which small pulses of biogenic opal increase the flux for no more than 1600 years at a time. The first pulse is at ~8900 ybp where the flux increases from 0.027 to 0.042 g/cm^2/kyr. The next pulse of opal is at ~5700 ybp where the flux jumps from 0.024 to 0.042 g/cm^2/kyr. The incidents of increased opal flux then slightly

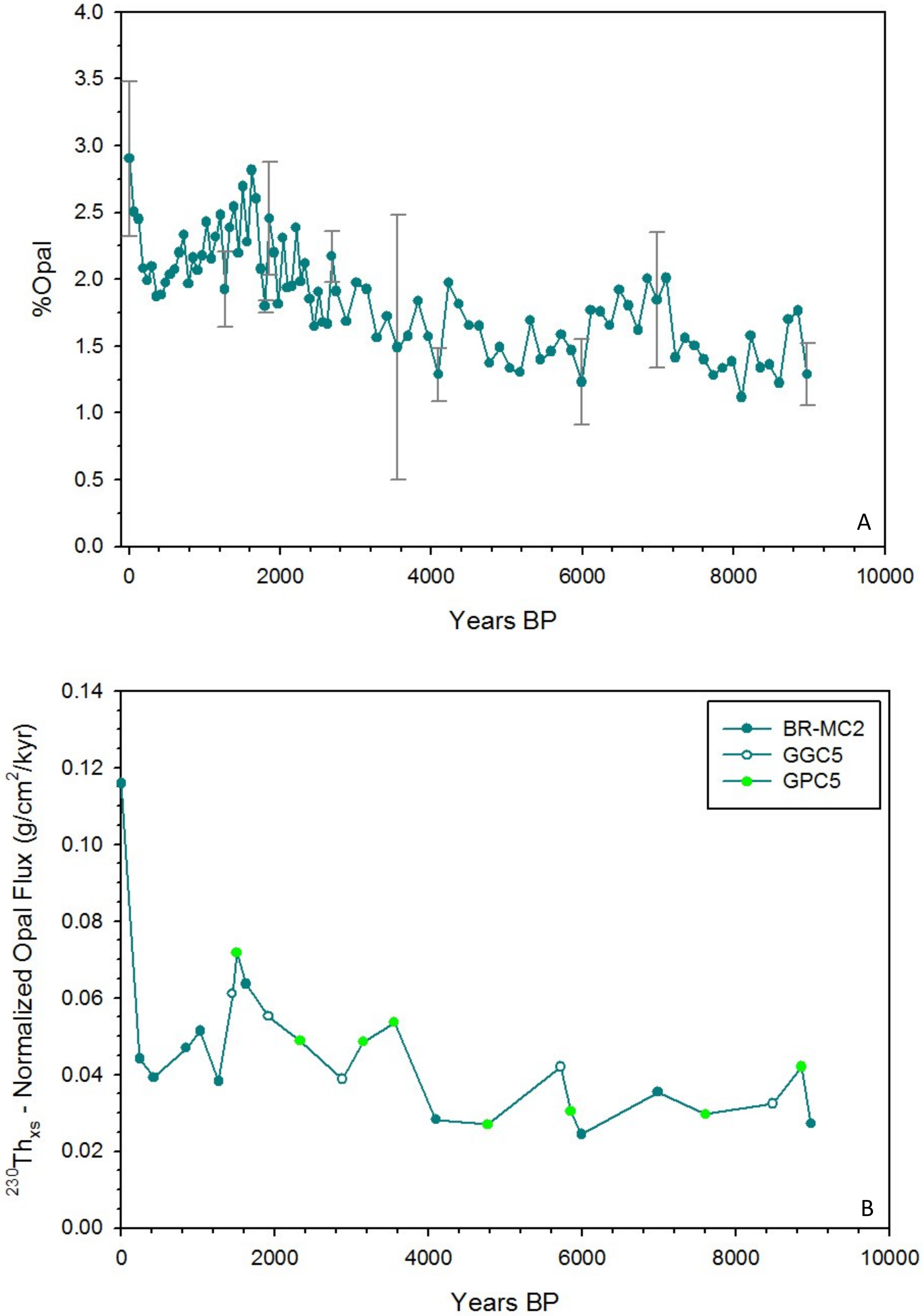

Figure 7. (A) %Opal with error bars signifying standard deviation (1σ) for replicated samples. (B) ^{230}Th normalized opal flux using sedimentary ^{230}Th$_{xs}$ values from BR-MC2, GGC5, and GPC5.

increase in magnitude as the next event at ~3600 ybp is an increase from 0.028 to 0.0536 g/cm^2/kyr and the one after that (~1500 ybp) is an increase from 0.039 to 0.072 g/cm^2/kyr. This is followed by the largest increase in opal flux, an increase from 0.044 to 0.116 g/cm^2/kyr at the present.

Sedimentary $^{231}Pa_{xs}/^{230}Th_{xs}$

The $^{231}Pa_{xs}/^{230}Th_{xs}$ record from GGC5 (McManus et al., 2004) has been used to supplement the data obtained from BR-MC2 for increased sample resolution (Figure 8). Note that the y-axis has been inverted to emphasize the inverse relationship between the ratio of $^{231}Pa_{xs}/^{230}Th_{xs}$ and the rate/intensity of Atlantic Meridional Overturning Circulation. $^{231}Pa_{xs}/^{230}Th_{xs}$ data from this study have values that are consistently less than the production ratio of 0.093 for the entirety of the Holocene and show some small-scale variations on an overall increasing trend toward the present. The $^{231}Pa_{xs}/^{230}Th_{xs}$ ratios remain within the range of 0.048–0.068. The early record is characterized by $^{231}Pa_{xs}/^{230}Th_{xs}$ ratios near 0.050 which increase to 0.061 quickly from ~5700–4800 ybp, then return to 0.048 by ~4100 ybp. From this point toward the present, there is a steady increase to 0.068 at the core top, interrupted by two small minima at ~1600 and 800 ybp (0.050 and 0.054, respectively).

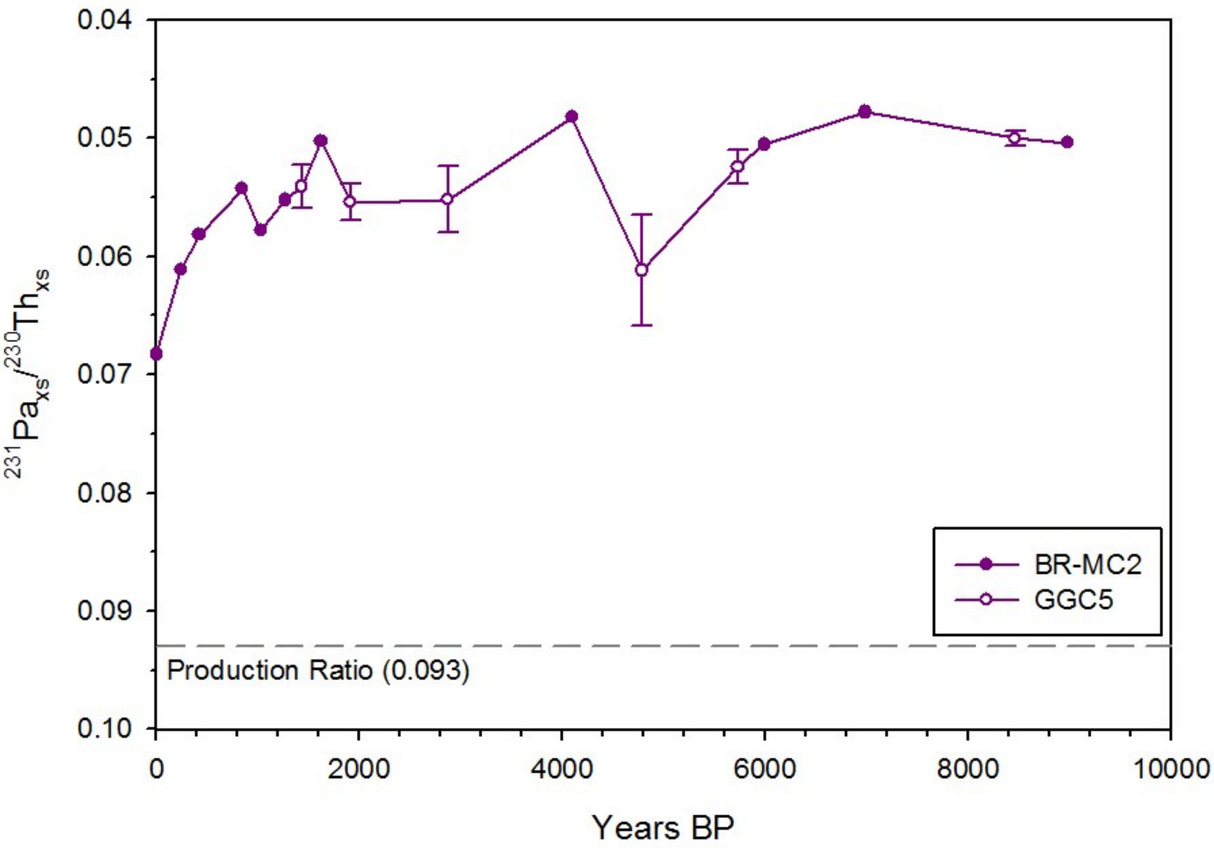

Figure 8. Excess, decay corrected $^{231}Pa/^{230}Th$ record compiled from BR-MC2 and GGC5. The dashed line marks the production ratio of $^{231}Pa_{xs}/^{230}Th_{xs}$ in the water column, 0.093. Error bars are those reported by McManus et al. (2004) for values obtained from core GGC5.

Discussion

This chapter reviews the results from BR-MC2 and discusses trends and possible interpretations in regards to both the climate record and biogenic opal effects on sedimentary $^{231}Pa_{xs}/^{230}Th_{xs}$.

Determination of Biogenic Opal Effect on Sedimentary $^{231}Pa_{xs}/^{230}Th_{xs}$

The affinity for biogenic opal to preferentially scavenge ^{231}Pa has been well established and documented globally in sediment trap, sediment core, and laboratory studies (Walter et al., 1997; Chase et al., 2002; Geibert and Usbeck, 2004; Luo and Ku, 2004; Siddall et al., 2005; Roberts et al., 2009). Previous sedimentary investigations in the Atlantic, however, have produced inconsistent results in terms of the actual impact of opal fluxes on the $^{231}Pa_{xs}/^{230}Th_{xs}$ record (McManus et al., 2004; Keigwin and Boyle, 2008; Gherardi et al., 2009; Lippold et al., 2009; Guihou et al., 2010).

McManus et al. (2004) (the study from which BR-MC2 data has been supplemented) have shown through the use of Si/Al ratios and visual inspection of samples for diatom frustules that there has been a negligible amount of opal flux to the Bermuda Rise during the last ~20 kyr. Any changes in opal flux during this interval in core GGC5 did not correlate with $^{231}Pa_{xs}/^{230}Th_{xs}$ ratios, thus supporting the proxy as a true record of Atlantic Meridional Overturning Circulation (AMOC) variability. Keigwin and Boyle (2008), however, revisited core GGC5 and brought in X-ray diffraction data from ODP site 1063 (also at the Bermuda Rise) and found opal flux at site 1063 to correlate with sedimentary $^{231}Pa_{xs}/^{230}Th_{xs}$ ratios during the Heinrich 1 (H1) (~17–15 kya). They suggest that there was a significant increase in opal flux to the Bermuda Rise during that time and $^{231}Pa_{xs}/^{230}Th_{xs}$ does not accurately reflect AMOC variability.

Gherardi et al. (2009) compiled sedimentary $^{231}Pa_{xs}/^{230}Th_{xs}$ data from six cores across the North Atlantic at varying depths: four deep cores [MD95-2027 (41°44' N, 47°44' W, 4112 m), SU90-44 (50°01' N, 17°06' W, 4279 m), GGC5 (McManus et al., 2004), and SU81-18 (37°46' N, 10°11' W, 3135 m)], one intermediate core [MD95-2037 (37°05' N, 32°01' W, 2150 m)], and one shallow core [DAPC2 (58°58' N, 09°36' W, 1709 m)].

In core MD95-2027, $^{231}Pa_{xs}/^{230}Th_{xs}$ values increased as both particle flux and diatom flux increased during H1. A similar occurrence happened during the Bølling-Allerød warm period (~15 kya) – particle flux increased as $^{231}Pa_{xs}/^{230}Th_{xs}$ values approached 0.093, suggesting that $^{231}Pa_{xs}/^{230}Th_{xs}$ data from this site may have been strongly influenced by particle flux, and thus might not accurately represent AMOC variations. The other three deep cores are more likely to provide more accurate sediment archives as the $^{231}Pa_{xs}/^{230}Th_{xs}$ records in cores SU90-44, GGC5, and SU81-18 did not covary with diatom or sediment flux. From the LGM (~19.8–17.5 kya) to H1, $^{231}Pa_{xs}/^{230}Th_{xs}$ values increased with constant particle fluxes in SU90-44 and GGC5. From the LGM to the beginning of the Holocene, the amount of diatoms decreased with a constant $^{231}Pa_{xs}/^{230}Th_{xs}$ and overall particle flux in core SU81-18. As the Holocene progressed the amount of diatoms decreased further and $^{231}Pa_{xs}/^{230}Th_{xs}$ values increased with no large change in overall particle flux.

Core MD95-2037 (the intermediate-depth core) showed a similar record to that of SU81-18, making it another credible $^{231}Pa_{xs}/^{230}Th_{xs}$ record. The shallow depth core, DAPC2, yielded more complicated results. From the LGM towards the Holocene, $^{231}Pa_{xs}/^{230}Th_{xs}$ values increased with decreasing particle flux and no change in diatom flux, indicating independent relationships. However, during the Holocene $^{231}Pa_{xs}/^{230}Th_{xs}$ increased slightly and remained high as the diatom flux increased, compromising the meaning of the ^{231}Pa$_{xs}$/^{230}Th$_{xs}$ data.

Similar to Keigwin and Boyle (2008), Lippold et al. (2009) revisited core GGC5 and ODP site 1063 to examine sediment from as far back as ~35 kya to the present. The diatom abundance and overall sediment flux data for ODP 1063 were found to be highly correlated with the combined ^{231}Pa$_{xs}$/^{230}Th$_{xs}$ records not only during H1, but the entire interval from ~35–14 kya. Lippold et al. hypothesized that the increased fluxes of diatoms during Heinrich events could actually have been the result of the intrusion of silica-rich AABW, a consequence of weakened AMOC. This is also supported by Dr. R. F. Anderson (as cited by Gil et al., 2009) who stated that these silica-rich waters (transported to the North Atlantic euphotic zone by cold-core rings or mode water eddies) could increase the scavenging of ^{231}Pa, resulting in higher ^{231}Pa$_{xs}$/^{230}Th$_{xs}$ values as an indirect response of decreased AMOC (Gil et al., 2009). Unfortunately these results conflict with McManus et al. (2004) and Gherardi et al. (2009) who declared the amount of silica flux negligible and supported the ^{231}Pa$_{xs}$/^{230}Th$_{xs}$ record of core GGC5.

Guihou et al. (2010) examined two North Atlantic cores, one from the western North Atlantic basin and one from the eastern North Atlantic basin (SU90-11: 44°04′ N, 40°01′ W, 3645 m and MD01-2446: 39°03′ N, 12°37′ W, 3547 m, respectively). Sampling back through the last glacial inception/MIS 5 (~127–60 kya), they found that the ^{231}Pa$_{xs}$/^{230}Th$_{xs}$ records were not significantly correlated with the opal records and can therefore be interpreted as changes in AMOC. The ^{231}Pa$_{xs}$/^{230}Th$_{xs}$ profiles also agreed with benthic □^{13}C and summer sea surface temperature (SST) data from other reference cores in each basin (summer SST is an indirect proxy for AMOC since it indicates the relative distribution of surface currents and therefore the transport of saline waters to sites of deep water formation).

The results of this study show a very weak correlation between the ^{231}Pa$_{xs}$/^{230}Th$_{xs}$ record and biogenic opal flux (Figure 9, A). When the data are plotted against each other, their correlation is represented by an r value of 0.62, implying about 38% of the variation in the $^{231}Pa_{xs}/^{230}Th_{xs}$ record is explained by variations in the opal record ($p = 0.0064$) (Figure 9, B). Although statistically significant, the correlation is clearly driven by the surface sample in which both datasets exhibit a rapid increase from ~200 ybp to the core top. To determine if the remainder of the sediment record exhibits the same correlation, the surface samples from both datasets were excluded. Their removal provides a much weaker correlation represented by $r = 0.17$ (Figure 9, C) and the relationship is no longer statistically significant ($p = 0.5020$), suggesting no effect of biogenic opal on sedimentary $^{231}Pa_{xs}/^{230}Th_{xs}$ during the majority of the Holocene.

A surface-driven correlation is also observed in the $^{231}Pa_{xs}/^{230}Th_{xs}$ data plotted with overall (^{230}Th-normalized) sediment flux. The correlation is represented by an r value of 0.55 which is only just statistically significant ($p = 0.0189$) (Figure 10, A and B). Excluding the surface sample from the datasets, the correlation also becomes insignificant with $p = 0.8516$ for a slightly negative correlation ($r = -0.05$) (Figure 10, C), suggesting that there is no effect of sediment flux on sedimentary $^{231}Pa_{xs}/^{230}Th_{xs}$ through the majority of the record.

Data generated from BR-MC2 alone were also analyzed for the aforementioned relationships to be sure that supplementing the dataset does not provide vastly different trends. Plotting BR-MC2 $^{231}Pa_{xs}/^{230}Th_{xs}$ with biogenic opal flux provided a correlation slightly stronger than the supplemented dataset with an r value of 0.75 ($p = 0.0050$) (Figure 11, A and B). However, the correlation is also surface-driven and removing surface samples produces another insignificant relationship ($r = 0.35$, $p = 0.2893$) (Figure 11, C). Plotting BR-MC2 $^{231}Pa_{xs}/^{230}Th_{xs}$ with sediment flux also shows a stronger correlation with an r value of 0.73 ($p = 0.0066$) (Figure

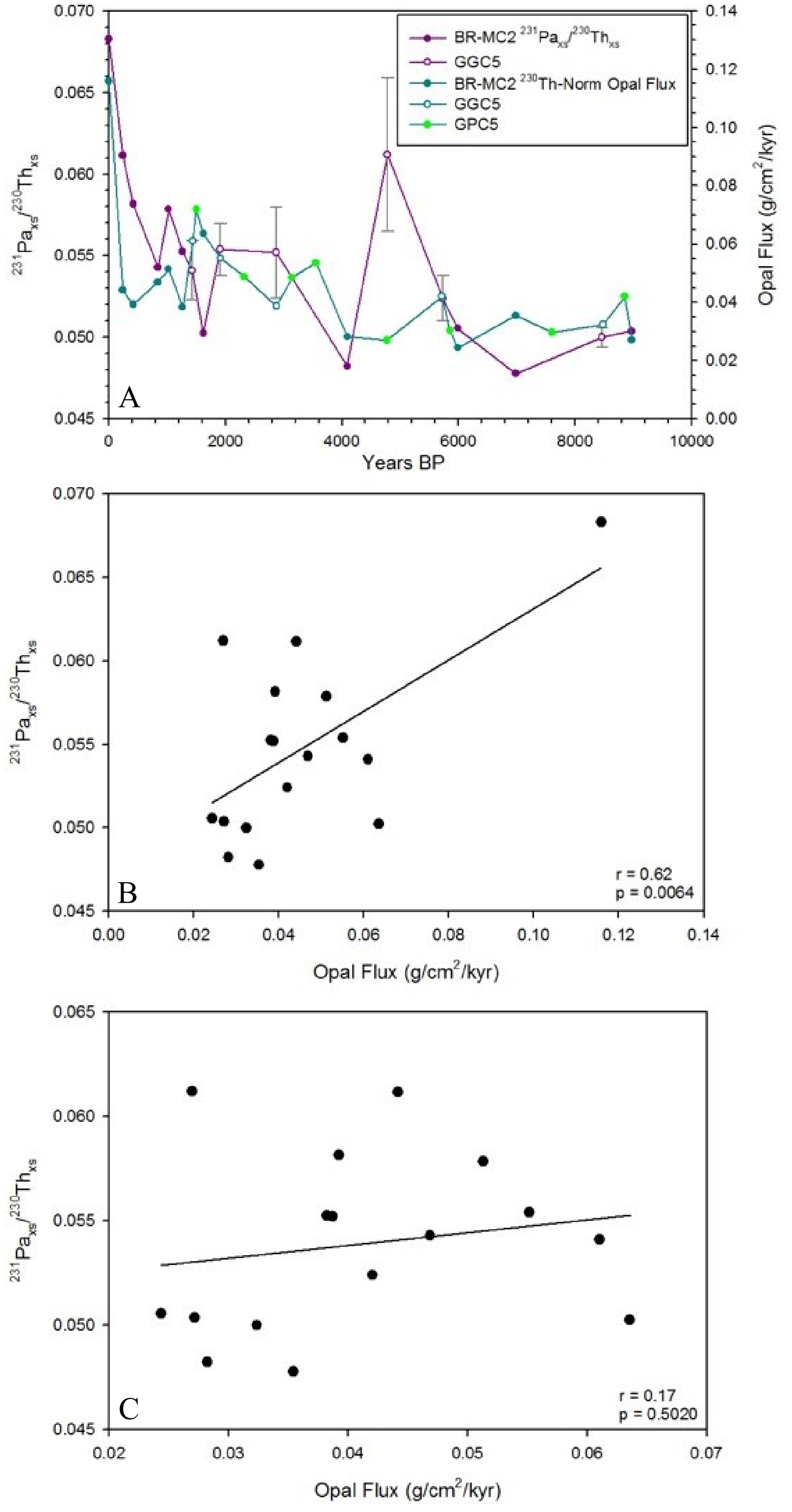

Figure 9. (A) Compiled excess ^{231}Pa/^{230}Th record plotted with ^{230}Th-normalized opal flux. Error bars mark those reported for GGC5 (McManus et al., 2004). (B) Correlation between the records with correlation coefficient and p-value (r = 0.62, p = 0.0064). (C) Correlation between records with surface samples removed (r = 0.17, p = 0.5020).

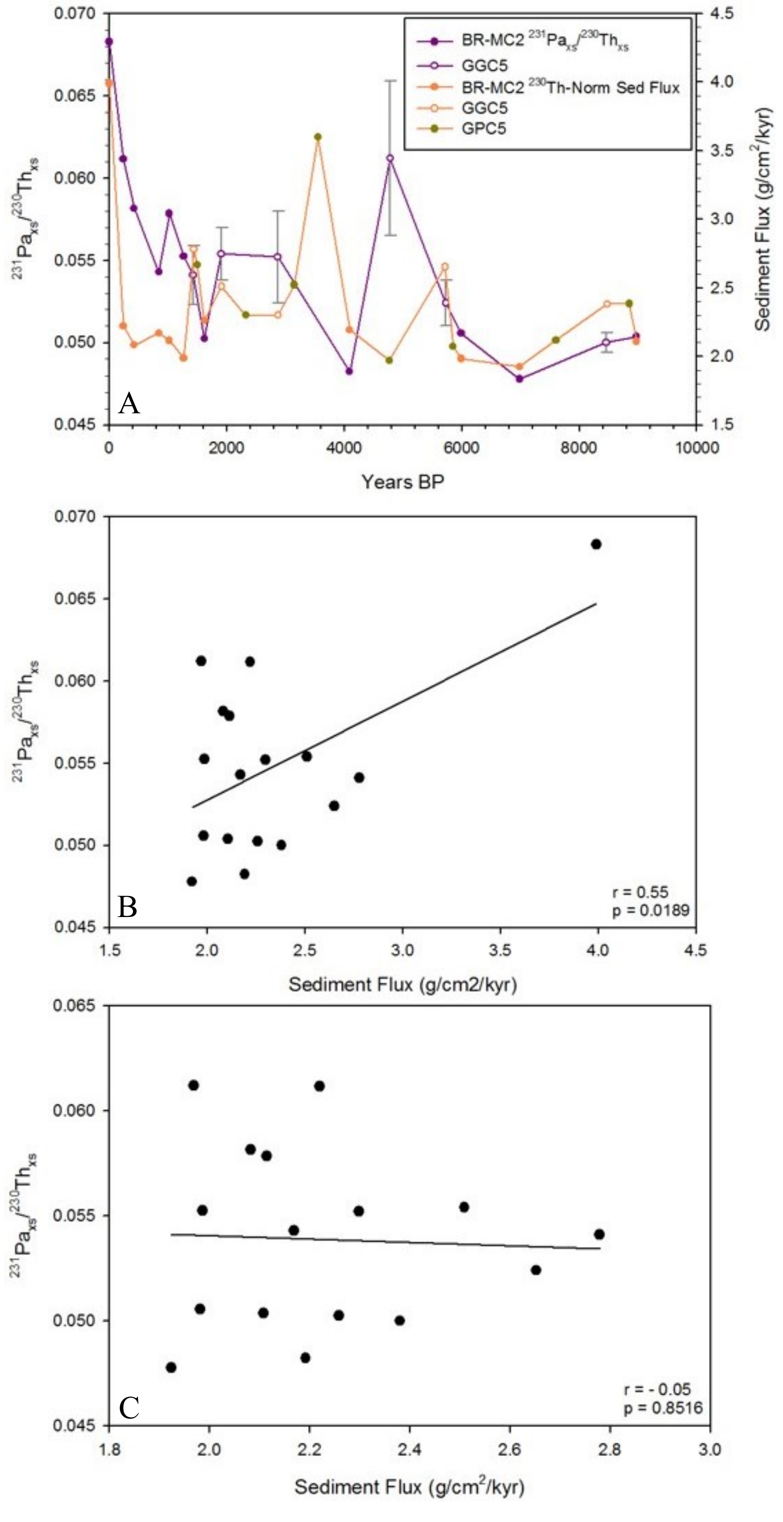

Figure 10. (A) Compiled excess ^{231}Pa/^{230}Th record plotted with ^{230}Th-normalized sediment flux. Error bars mark those reported for GGC5 (McManus et al., 2004) (B) Correlation between the records with correlation coefficient and p-value (r = 0.55, p = 0.0189). (C) Correlation between records with surface samples removed (r = -0.05, p = 0.8516).

12, A and B). Again, the correlation is forced by the surface sample, and removing said sample provides an insignificant correlation ($r = 0.23$, $p = 0.4876$) (Figure 12, C). Similar surface-driven relationships between BR-MC2 and supplemented datasets support the conclusion that both opal and sediment flux have no significant effect on sedimentary $^{231}Pa_{xs}/^{230}Th_{xs}$ through most of the Holocene.

The overall lack of correlation in this study is in agreement with the results of the previously mentioned $^{231}Pa_{xs}/^{230}Th_{xs}$ versus opal flux studies for data spanning the last ~10 kya (McManus et al., 2004; Keigwin and Boyle, 2008; Gherardi et al., 2009; Lippold et al., 2009; Guihou et al., 2010). Here, it is evident that $^{231}Pa_{xs}/^{230}Th_{xs}$ is not significantly influenced by biogenic opal flux, or total sediment flux during the majority of the Holocene. The lack of correlation between sedimentary opal and $^{231}Pa_{xs}/^{230}Th_{xs}$ suggests that Bermuda Rise sediments are a robust archive of past AMOC variability. However, it is also possible that the relatively low amount of biogenic silica found in the sediments are insufficient to impact $^{231}Pa_{xs}/^{230}Th_{xs}$ over the length of this study. I cannot rule out the possibility that higher opal fluxes in the past (e.g., the LGM) would not have impacted the $^{231}Pa_{xs}/^{230}Th_{xs}$ record being deposited at that time.

The surface samples from my study could reflect a compositional effect of biogenic opal on the $^{231}Pa_{xs}/^{230}Th_{xs}$ record. This is the only sample which exhibits such a rapid increase of opal flux to such a high level; it is almost double the amount of the next highest opal flux in the entire Holocene record. The correlation between $^{231}Pa_{xs}/^{230}Th_{xs}$ and sediment flux in this sample also supports a compositional effect. Increased particle flux in the North Atlantic is not a major concern due to the residence time of the waters in the basin (100–200 years); there isn't enough time to allow for sufficient accumulation of particles that impacts the fractionation between ^{231}Pa and ^{230}Th (Yu et al., 1996). Therefore, the reason for the correlation is most likely due to the

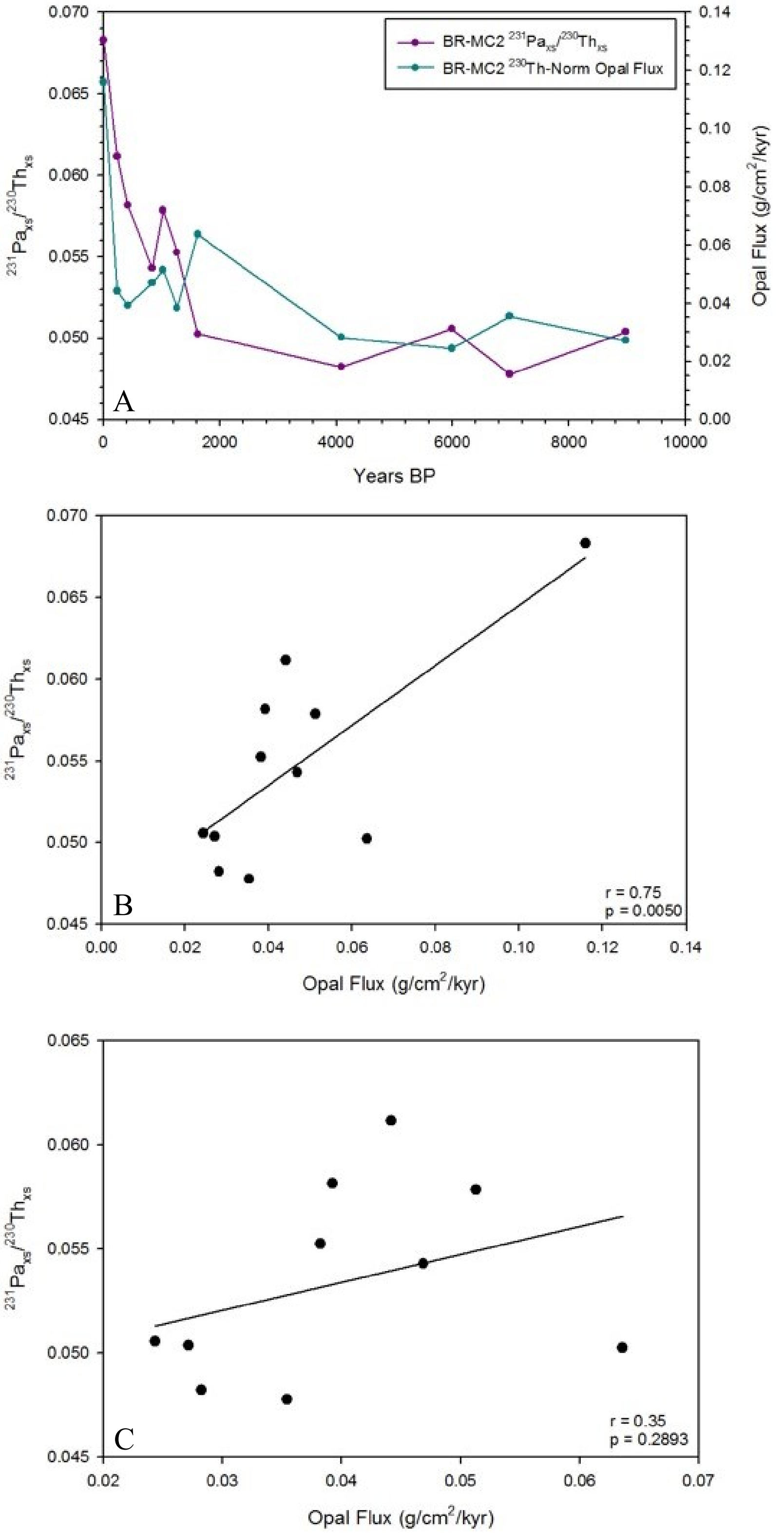

Figure 11. (A) BR-MC2 excess $^{231}Pa/^{230}Th$ record plotted with ^{230}Th-normalized opal flux. (B) Correlation between the records with correlation coefficient and p-value ($r = 0.75$, $p = 0.0050$). (C) Correlation between records with surface samples removed ($r = 0.35$, $p = 0.2893$).

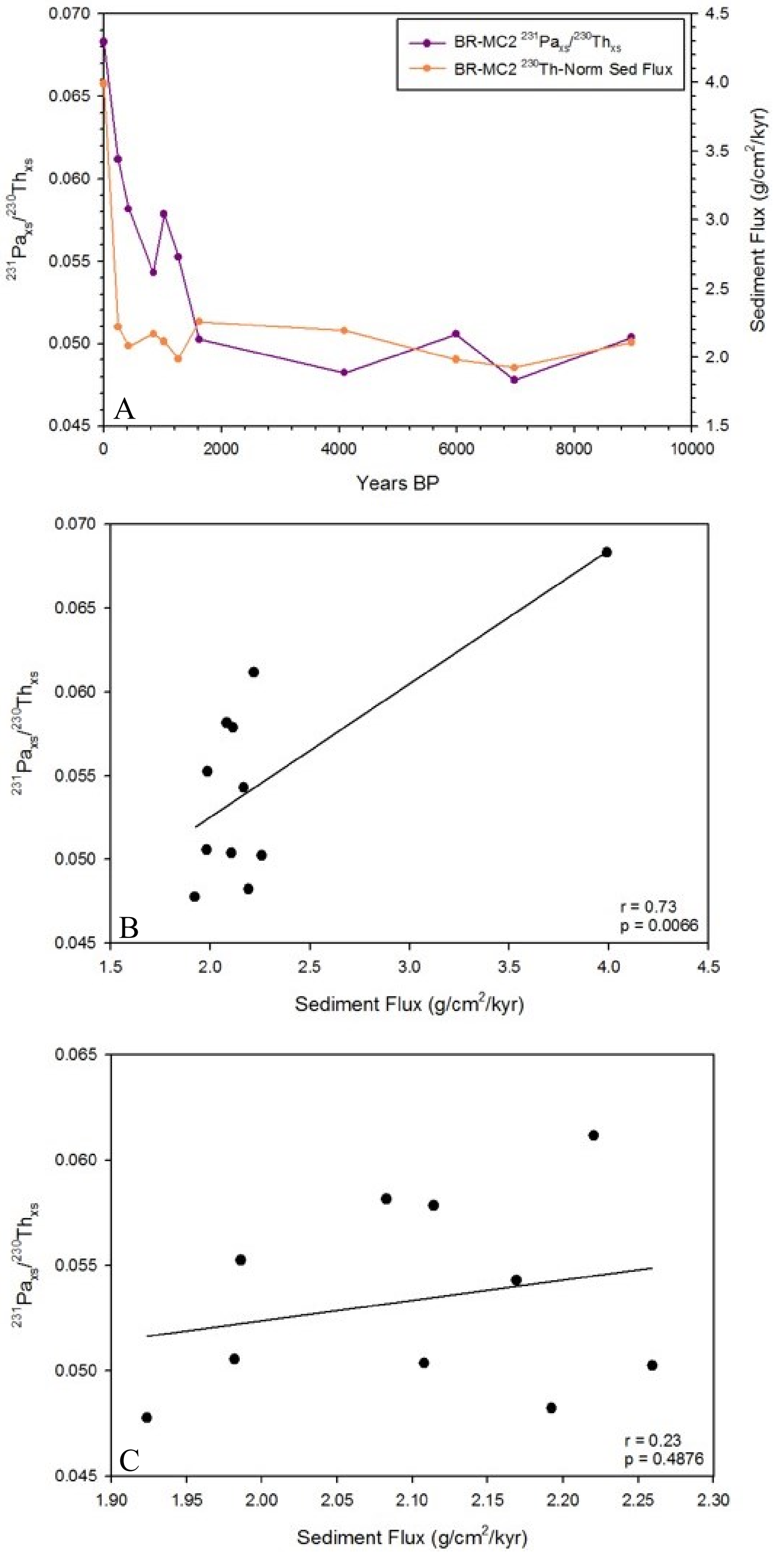

Figure 12. (A) BR-MC2 excess ^{231}Pa/^{230}Th record plotted with ^{230}Th-normalized sediment flux. (B) Correlation between the records with correlation coefficient and p-value (r = 0.73, p = 0.0066). (C) Correlation between records with surface samples removed (r = 0.23, p = 0.4876).

composition of the increased particle flux.

It should be noted that the surface samples are also associated with a sampling error that could have affected the value of $^{231}Pa_{xs}/^{230}Th_{xs}$ and/or opal flux. The surface/core-top sample was not homogenized before an aliquot was taken for radionuclide or silica analysis, which could have resulted in anomalously high values by sampling from a pocket of increased opal content. Another source of error for the biogenic opal measurements was the methodology. The silica was extracted using a 2M Na_2CO_3 solution in order to leach all of the biogenic opal from the sediments (Mortlock and Froelich, 1989). Silica can become more impervious to leaching as it ages, so the stronger 2M solution helps with older sediments, but it can also have an adverse effect and leach silica from clay leading to a misinterpretation of the biogenic phase of silica (Shemesh et al., 1988).

To determine if the opal flux is produced in the surface waters of the Bermuda Rise or being laterally transported, the planktonic foraminiferal $\delta^{13}C$ can be compared to the opal record. Increased primary production in the surface waters would fractionate the stable carbon isotopes leaving the water isotopically heavy as the lighter ^{12}C is preferentially taken up during photosynthesis by phytoplankton (Ruddiman, 2008). Foraminifera living in the surface waters during intervals of high productivity would produce carbonate tests relatively enriched in ^{13}C, and thus there should be a positive correlation between the $\delta^{13}C$ and opal flux records.

From the early Holocene (~9000 ybp) the overall trend of the $\delta^{13}C$ record parallels that of the opal flux until ~3600 ybp where the records clearly diverge for a period of ~1500 yr (Figure 13). The records then resume a rough correlation towards the present. The periods of correlation and lack of correlation suggest that the opal is in fact being produced locally with the exception of the ~1500 yr interval. However, this is based on the assumption that siliceous

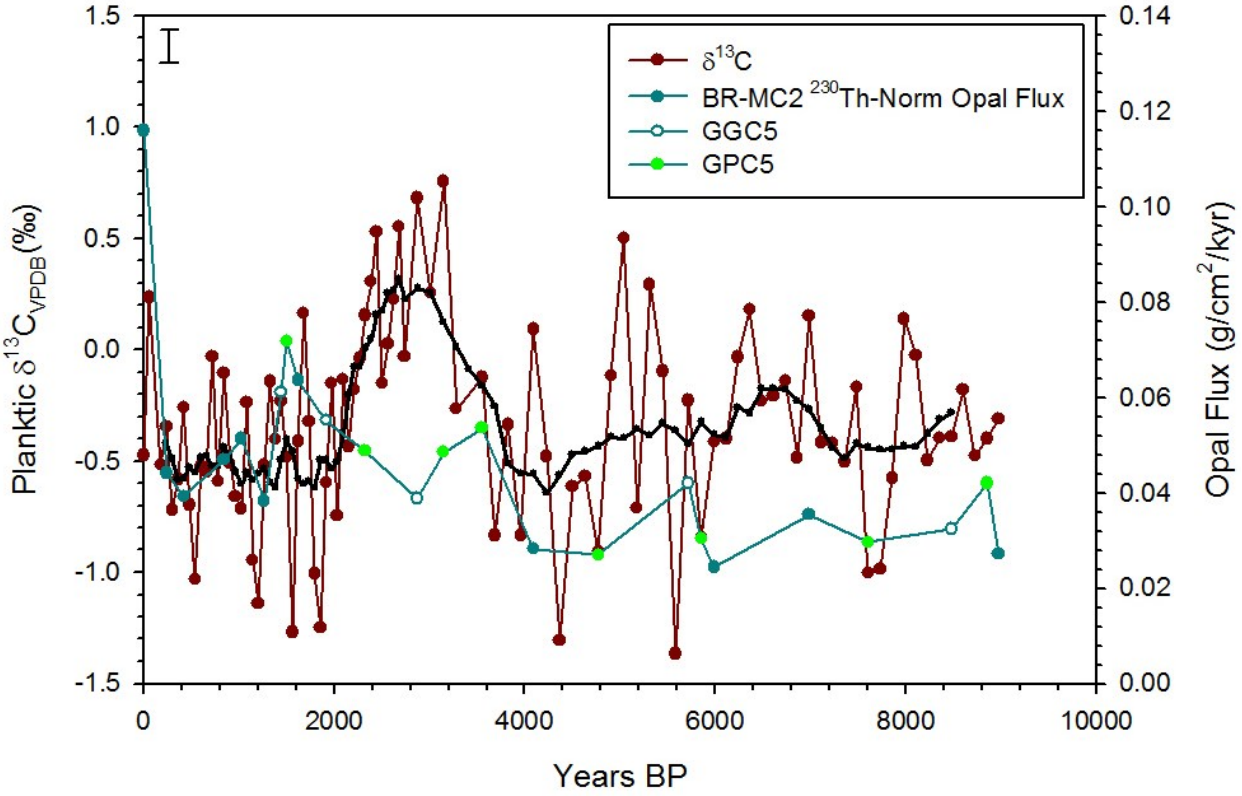

Figure 13. Planktic $\delta^{13}C$ from BR-MC2 (with 9-point running average overlain) plotted with compiled ^{230}Th normalized biogenic opal flux. Error bar in the top left corner notes the ± 0.06‰ (1σ) error associated with the analytical precision of the standard.

phytoplankton are the driving force behind primary production in the surface waters of the Bermuda Rise. There are many other primary producers such as coccolithophores which produce calcium carbonate tests (Garrison, 2009), and production by these organisms at the expense of diatoms could skew the opal- $\delta^{13}C$ relationship.

Interpretations of AMOC Changes through the Holocene

With the caveats of potential opal flux influence on $^{231}Pa_{xs}/^{230}Th_{xs}$ in the core surface sample and the previously-noted age model concerns about the same sample, the remaining sedimentary $^{231}Pa_{xs}/^{230}Th_{xs}$ record can be interpreted as true changes in AMOC as observed at the Bermuda Rise through the Holocene. The overall record implies steady circulation rates with a mean Holocene $^{231}Pa_{xs}/^{230}Th_{xs}$ of 0.055. There is also a small maximum at ~4800 ybp and a steady increase ~800 ybp to the present, indicating that there could be a slightly weakened AMOC in which values increase from 0.052 to 0.061, then 0.054 to 0.068, respectively (Figure 14, A). The first maximum is roughly 50% of the $^{231}Pa_{xs}/^{230}Th_{xs}$ change characterizing the AMOC slow-down during the Younger Dryas (YD) cooling event (McManus et al., 2004), while the increase towards the present is about 80% of the YD. It must be noted that the first maximum is from core GGC5 and is associated with a relatively large error, but even with the error indicates a partial slowing of AMOC (McManus et al., 2004).

The interpreted changes in AMOC intensity are supported by benthic $\delta^{13}C$ data compiled from two cores at the Bermuda Rise (GPC5 [Keigwin et al., 1991] and BC-004D [Keigwin, 1996]), reinforcing that they are being controlled by a common forcing mechanism: AMOC (Keigwin et al., 1991) (Figure 14, B). These data show the same small-magnitude shift at ~5000 ybp where $\delta^{13}C$ decreases by ~0.2‰, but the change toward the present is much more drastic

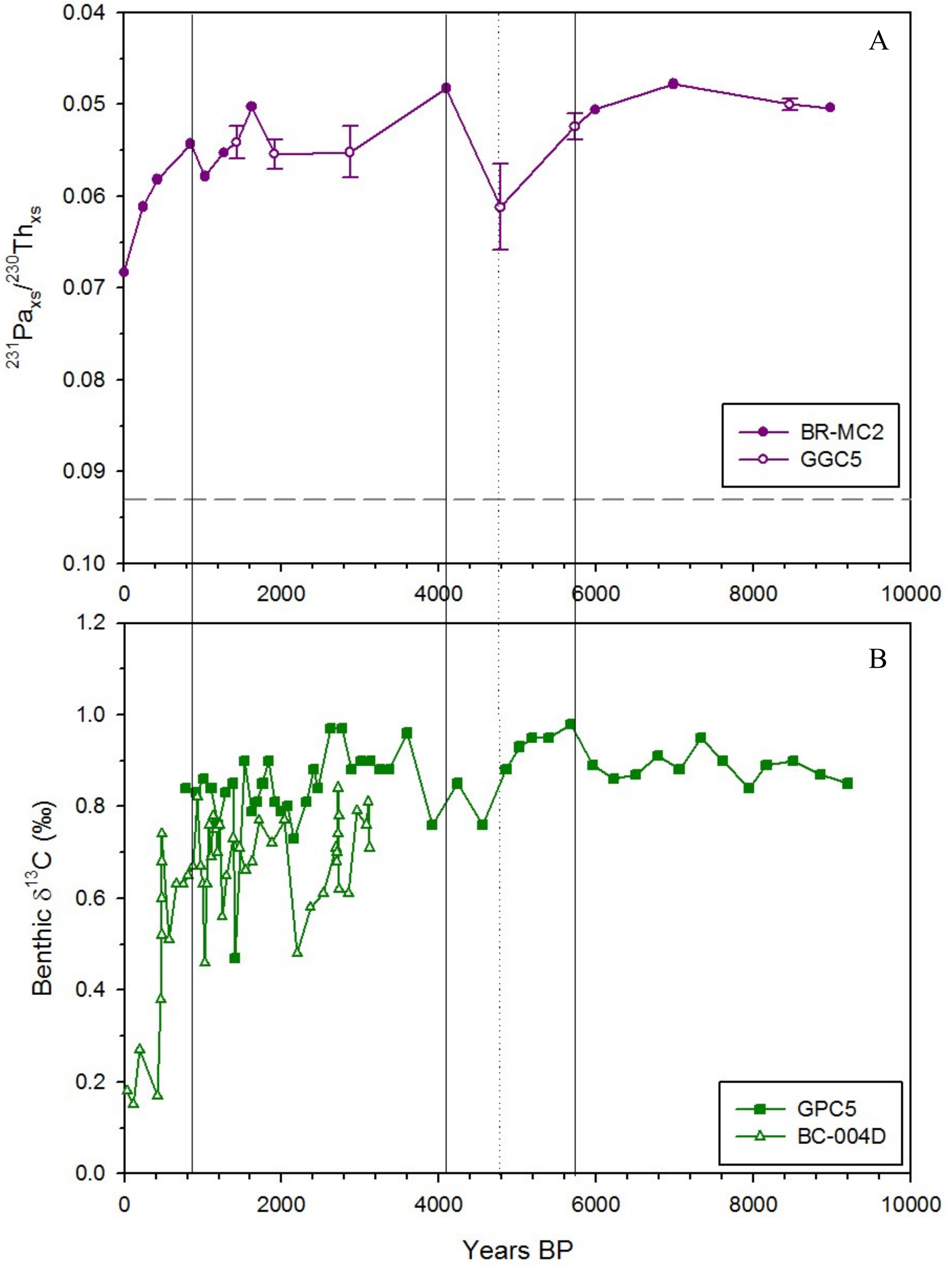

Figure 14. (A) $^{231}Pa_{xs}/^{230}Th_{xs}$ record from BR-MC2 and GGC5 with the production ratio (0.093) marked by the dashed line. Error bars are displayed as reported by McManus et al. (2004) for core GGC5. Note the y-axis is inverted to signify increasing AMOC upward and weakening, downward (B) Benthic $\delta^{13}C$ data from GPC5 and BC-004D. The solid reference lines mark intervals of decreased AMOC according to the $^{231}Pa_{xs}/^{230}Th_{xs}$ record (from ~5700–4100 ybp and from ~800 ybp to present). The dotted line marks the minimum of AMOC as represented by the $^{231}Pa_{xs}/^{230}Th_{xs}$ record.

with a decrease of ~0.6‰. The first decreases implies a weakening of overturning circulation by a higher proportion of ^{12}C-enriched bottom waters, but the second suggests a near shut-down as the δ^{13}C reaches a value characteristic of southern-source waters (Keigwin and Boyle, 2000). The drastic decrease in the benthic δ^{13}C values could also be an artifact of an increased rain of lighter ^{12}C (Keigwin and Boyle, 2000). With increased production in surface waters, the organic material rains to the deep waters and decays, supplying lighter ^{12}C to the dissolved inorganic pool of carbon from which the benthic foraminifera construct their tests. This is supported by the increased opal flux recorded in BR-MC2 near the present (Figure 13).

Comparing $^{231}Pa_{xs}/^{230}Th_{xs}$ and δ^{13}C to compiled benthic foraminiferal Cd/Ca data (cores GGC1 [Boyle and Keigwin, 1987], BC-004A, and BC-004D [Keigwin, 1996]) complicates the interpretation of AMOC changes further. In core GGC1, Cd/Ca exhibits a large increase from 0.077 to 0.111 that coincides with the early AMOC slow-down interval (~5300 ybp), but values quickly drop back to 0.073 by the time the peak $^{231}Pa_{xs}/^{230}Th_{xs}$ value is reached. Towards the present, core BC-004A exhibits a slight Cd/Ca increase of 0.011, indicating a small decrease in the strength of AMOC as nutrient-rich waters become slightly more prominent, but it is not the same magnitude of an increase that would be expected with such a large decrease in benthic δ^{13}C (Figure 15, A) (Keigwin and Boyle, 2000). Core BC-004D surface samples display a decrease of Cd/Ca by 0.033 which implies more rapid circulation as bottom waters are becoming nutrient-poor. A possible explanation for the decreasing values in BC-004D that disagree with Cd/Ca in other cores could be that the most abundant benthic foraminifer used in Cd/Ca measurements was *Cibicidoides wuellerstorfi*, which is vulnerable to decreased values of Cd/Ca when there is $CaCO_3$ dissolution (Keigwin and Boyle, 2000). Dissolution is more likely to occur when there is an increased presence of corrosive AABW due to reduced circulation, so decreased Cd/Ca could

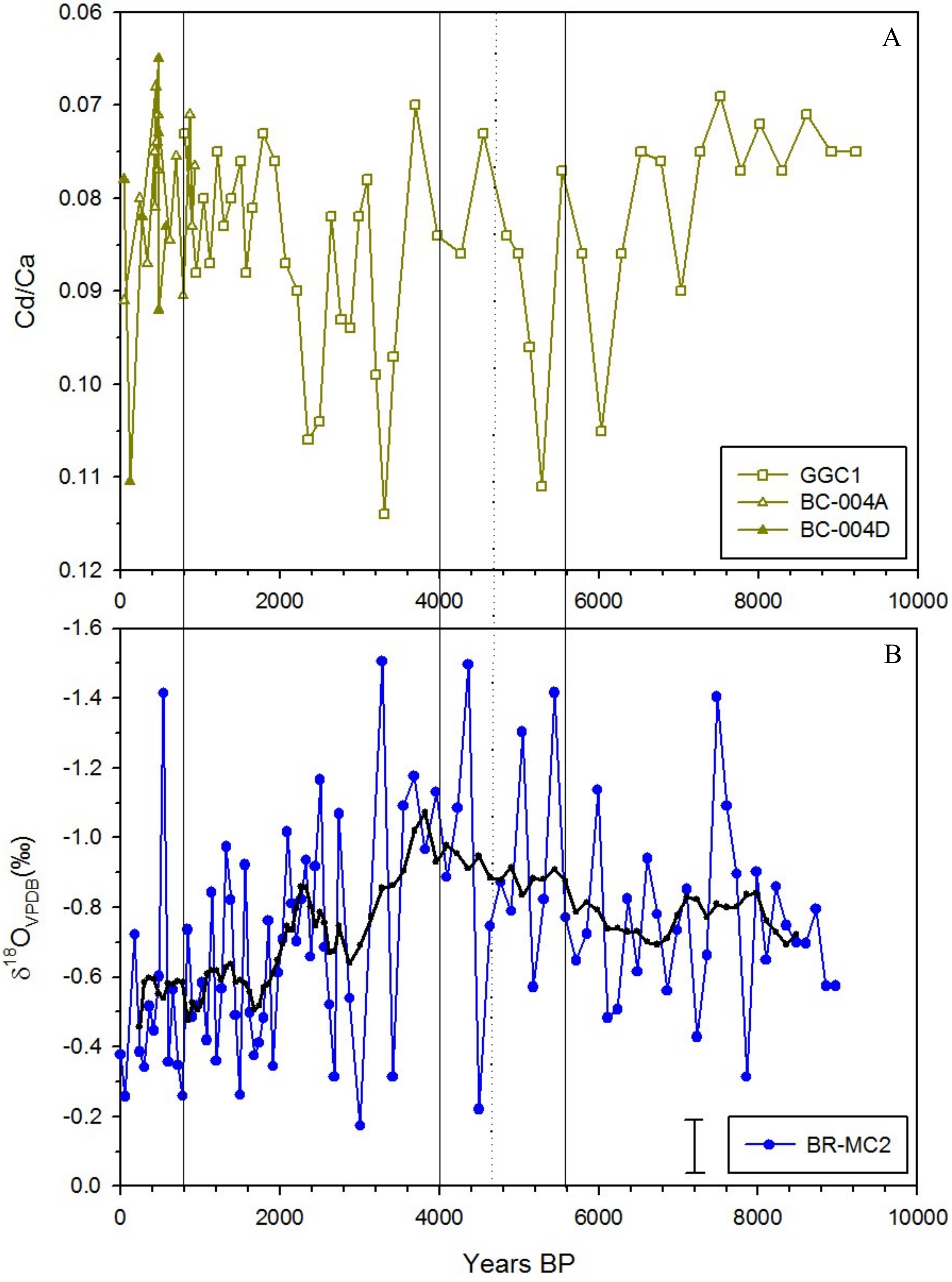

Figure 15. (A) Cd/Ca data from GGC1, BC-004A, and BC-004D. (B) $\delta^{18}O$ data from BR-MC2 with 9-point running average, and an error bar near the legend noting ± 0.08‰ error associated with the analytical precision of the standard. Note that the y-axes are inverted to signify increasing AMOC upward and weakening, downward. The solid and dotted reference lines mark the same intervals noted in Figure 14.

actually be the record of declining AMOC.

Planktonic foraminiferal $\delta^{18}O$ is a proxy for sea surface temperature and salinity, and thus acts as an indicator for warm, saline waters being present in the subtropics as a direct result of AMOC surface limb intensity. Therefore, planktonic foraminiferal $\delta^{18}O$ from BR-MC2 can be added to the list of possible indirect proxies for the strength of circulation at the Bermuda Rise (Adkins et al., 1997). The $\delta^{18}O$ record shows values around -0.9‰ that actually become more negative, reaching -1.0‰ during the interval of assumed slower circulation. This signal reflects an increase in temperature that could be associated with increased delivery of warmer waters by strengthening AMOC (Figure 15, B). However, the $\delta^{18}O$ is not significantly lower before this time interval, so there is no indication of the initial slowing of AMOC. The slowing of circulation on the more recent interval (~800 ybp to the present) is more evident in the $\delta^{18}O$ record; average $\delta^{18}O$ values during this time become less negative which is evidence for cooling surface temperatures that could result from lessened delivery of warm equatorial waters. Unfortunately, this cooling trend in the planktic $\delta^{18}O$ has been established for roughly the last 4000 years, suggesting that it is not a response to AMOC variability.

Holocene Climate Variability from BR-MC2 Sediments

The Holocene can be divided into two temperature-based climate intervals: the Hypsithermal and the Neoglaciation. The Hypsithermal is characterized by warmer mean temperatures and occurs from just after 11 kya and continues until ~5 kya (Keigwin, 1996; Deevey and Flint, 1957). After ~5 kya, temperatures begin an overall decrease towards the present, known as the Neoglaciation (Keigwin, 1996). Both periods are evident in the planktonic foraminiferal $\delta^{18}O$ record from BR-MC2; the Hypsithermal is characterized by an average $\delta^{18}O$

of -0.78‰ and the Neoglaciation exhibits a less negative average $\delta^{18}O$ of - 0.68‰ (Figure 16).

In the early Holocene, the Hypsithermal was interrupted by the brief 8.2 ky event which is characterized by a rapid decrease in North Atlantic sea surface temperatures of ~2°C roughly 8.2 kya, and is thought to have been caused by a change in AMOC due to meltwater pulse to the Atlantic (Barber et al., 1999). Unfortunately, my data does resolve this event in either the $\delta^{18}O$ or $^{231}Pa_{xs}/^{230}Th_{xs}$ records.

In the late Holocene, the Medieval Climate Anomaly (MCA) interrupted the Neoglaciation by warming briefly from ~850-650 ybp which was only recorded in several locations around Europe and high latitudes in the North Atlantic (Ruddiman, 2008). The MCA doesn't seem to be recorded in the planktic $\delta^{18}O$ record at this time (Figure 16). The data show a small shift toward lighter values at ~800 ybp from -0.5‰ to -0.6‰, but this is not a unique event. There are similar magnitude shifts in average $\delta^{18}O$ values for the last ~2000 years. Using the timescale of Keigwin (1996) who suggests the MCA was closer to 1000 ybp, these data actually show a cooling trend in which values become less negative (-0.6‰ to -0.5‰) for this time period.

More recently, the Little Ice Age (LIA) was a cooling event after the MCA (from ~500-300 ybp) that was also more frequently resolved in climate data in higher latitudes (Ruddiman, 2008). This time interval coincides with Keigwin's (1996) description of the LIA, and is marked in the average $\delta^{18}O$ values near -0.6‰ (~500 ybp) that become slightly heavier, reaching -0.5‰ (~200 ybp) (Figure 16). Similar to the MCA, the signal for the LIA is not unique and both climate events also occur within the depths of bioturbated surface samples in BR-MC2, which could be muting a stronger climate signal. The MCA and LIA, although marked by the proper change in planktic foraminiferal $\delta^{18}O$, are not strongly marked in the BR-MC2 sediment record.

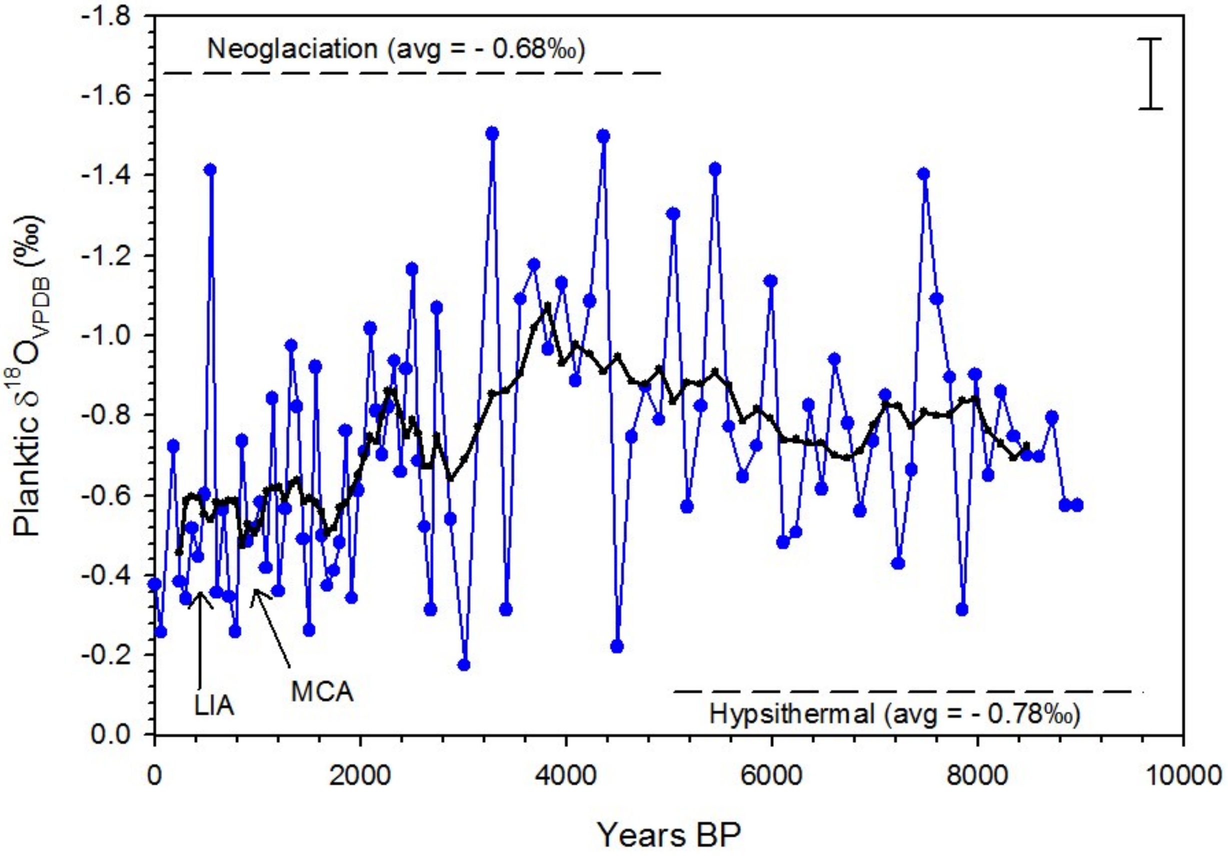

Figure 16. Planktonic foraminiferal $\delta^{18}O$ from BR-MC2 overlain with 9-point running average. Note the inverted y-axis to illustrate changes in temperature during the Holocene. Error bar in the top right corner notes the ± 0.08‰ (1σ) error associated with the analytical precision of the standard. Overlain on the plot are climate events of the Holocene (LIA = Little Ice Age, MCA = Medieval Climate Anomaly) after Keigwin (1996).

Conclusions

This study has provided additional data that creates the highest resolution $^{231}Pa_{xs}/^{230}Th_{xs}$ record spanning the Holocene to date at the Bermuda Rise. Comparison of this new record with biogenic opal flux suggests that there is little significant correlation over the interval of study, and that the ratio of radionuclides can be reliably interpreted as changes in deep ocean circulation. The only existing correlation between biogenic opal flux and $^{231}Pa_{xs}/^{230}Th_{xs}$ values in this dataset is at the surface, implying a compositional effect that is supported by comparison with benthic $\delta^{13}C$ from a nearby sediment record. Since these are the only correlated samples, and opal flux reaches its highest values during this recent interval, it follows that there could be a threshold of biogenic opal flux that was reached for there to be sufficiently increased ^{231}Pa scavenging to impact the interpretation of down-core $^{231}Pa_{xs}/^{230}Th_{xs}$ data.

However, due to the presence of a bioturbated mixed layer, the entire trend of increasing $^{231}Pa_{xs}/^{230}Th_{xs}$ from ~800 ybp towards the present should be interpreted as enhanced ^{231}Pa scavenging driven by a pulse of increased opal flux. The bioturbated layer also raises concerns with the age model from which data was interpreted in this study. Future analyses should include an adjusted age model assuming a constant age for the mixed layer and linear interpolation based on a best-fit line through the rest of the dated depths, providing a more accurate representation of the timeline for the BR-MC2 sediment record.

Interpretation of the remainder of the $^{231}Pa_{xs}/^{230}Th_{xs}$ record as circulation variability indicates that AMOC is relatively stable during the Holocene with one interval of marked weakening. Although this interval is associated with the largest error and there are notable disagreements with other paleocirculation proxies for this time, increased sampling resolution and determination of $^{231}Pa_{xs}/^{230}Th_{xs}$ ratios around this interval would provide information as to the actual changes in AMOC. Sampling across the Atlantic and Southern Oceans would also provide a more cohesive picture of basin-wide AMOC variability.

References

Adkins, J. F., Boyle, E. A., Keigwin, L. D., and Cortijo, E. (1997). Variability of the North Atlantic thermohaline circulation during the last interglacial period. *Nature*, *390*, 154-156.

Anderson, H. L., Francois, R., and Moran, S. B. (1992). Experimental evidence for differential adsorption of Th and Pa on different particle types in seawater. *Eos, Trans. AGU*, *73*, 270.

Anderson, R. F., Bacon, M. P., and Brewer, P. G. (1983). Removal of ^{230}Th and ^{231}Pa from the open ocean. *Earth and Planetary Science Letters*, *62*, 7-23.

Ayer, E. A., and Laine, E. P. (1982). Seismic stratigraphy of the northern Bermuda Rise. *Marine Geology*, *49*(1), 169-186.

Bacon, M. P. (1984). Glacial to interglacial changes in carbonate and clay sedimentation in the Atlantic Ocean estimated from ^{230}Th measurements. *Chemical Geology*, *46*(2), 97-111.

Bacon, M. P., Roether, W., and Elderfield, H. (1988). Tracers of chemical scavenging in the ocean: boundary effects and large-scale chemical fractionation [and discussion]. *Philosophical Transactions of the Royal Society of London. Series A, Mathematical and Physical Sciences*, *325*(1583), 147-160.

Barber, D. C., Dyke, A., Hillaire-Marcel, C., Jennings, A. E., Andrews, J. T., Kerwin, M. W., Bilodeau, G., McNeely, R., Southon, J., Morehead, M. D., and Gagnon, J. M. (1999). Forcing of the cold event of 8,200 years ago by catastrophic drainage of Laurentide lakes. *Nature*, *400*, 344-348.

Bianchi, G. G. and McCave, I. N. (1999). Holocene periodicity in North Atlantic climate and deep-ocean flow south of Iceland. *Nature*, *397*, 515-517.

Boyle, E. A. and Keigwin, L. D. (1987). North Atlantic thermohaline circulation during the past 20,000 years linked to high-latitude surface temperature. *Nature*, *330*, 35-40.

Broecker, W. S. (2000). Was a change in thermohaline circulation responsible for the Little Ice Age? *Proceedings of the National Academy of Sciences*, *97*, 1339-1342.

Chase, Z., Anderson, R. F., Fleisher, M. Q., and Kubik, P. W. (2002). The influence of particle composition and particle flux on scavenging of Th, Pa and Be in the ocean. *Earth and Planetary Science Letters*, *204*, 215-229.

Cheng, H., Edwards, R. L., Hoff, C. D., Richards, D. A., and Asmerom, Y. (2000). The half-lives of uranium-234 and thorium-230. *Chemical Geology*, *169*, 17-33.

Curry, W. B. and Oppo, D. W. (2005). Glacial water mass geometry and the distribution of δ^{13}C of ΣCO_2 in the western Atlantic Ocean. *Paleoceanography*, *20*(1).

Deevey, E. S. and Flint, R. F. (1957). Postglacial hypsithermal interval. *Science*, *125*(3240), 182-184.

Fairbanks, R. G. (1989). A 17,000-year glacio-eustatic sea level record: influence of glacial melting rates on the Younger Dryas event and deep-ocean circulation, *Nature*, *342*, 637-642.

Francois R., Frank, M., Rutgers van der Loeff, M. M., and Bacon, M. P. (2004). ^{230}Th normalization: an essential tool for interpreting sedimentary fluxes during the late Quaternary. *Paleoceanography*, *19*(1).

Garrison, T. S. (2009) Essentials of oceanography (5th ed.). Belmont, CA: Brooks/Cole Cengage Learning.

Geibert, W. and Usbeck, R. (2004). Adsorption of thorium and protactinium onto different particle types: experimental findings. *Geochimica et Cosmochimica Acta*, *68*(7), 1489-1501.

Gherardi, J. M., Labeyrie, L., McManus, J. F., Francois, R., Skinner, L. C., and Cortijo, E. (2005) Evidence from the Northeastern Atlantic basin for variability in the rate of the meridional overturning circulation through the last deglaciation. *Earth and Planetary Science Letters*, *240*, 710-723.

Gil, I. M., Keigwin, L. D., and Abrantes, F. G. (2009). Deglacial diatom productivity and surface ocean properties over the Bermuda Rise, northeast Sargasso Sea. *Paleoceanography*, *24*(4).

Guihou, A., Pichat, S., Nave, S., Govin, A., Labeyrie, L., Michel, E., and Waelbroeck, C. (2010). Late slowdown of the Atlantic Meridional Overturning Circulation during the Last Glacial Inception: new constraints from sedimentary (^{231}Pa/^{230}Th*). Earth and Planetary Science Letters*, *289*, 520-529.

Guo, L., Chen, M., and Gueguen, C. (2002). Control of Pa/Th ratio by particulate chemical composition in the ocean. *Geophysical Research Letters*, *29*(20), 22-1.

Harvey, L. D. D. (1989). Modelling the Younger Dryas. *Quaternary Science Reviews*, *8*(2), 137-149.

Henderson, G. M. (2002). New oceanic proxies for paleoclimate. *Earth and Planetary Science Letters*, *203*, 1-13.

Henderson, G. M. and Anderson, R. F. (2003). The U-series toolbox for paleoceanography. *Reviews in Mineralogy and Geochemistry*, *52*, 493-531.

Jaffey, A. H., Flynn, K. F., Glendenin, L. E., Bentley, W. T., and Essling, A. M. (1971). Precision measurement of half-lives and specific activities of U 235 and U 238. *Physical Review C*, *4*, 1889.

Keigwin, L.D. (1996). The Little Ice Age and Medieval Warm Period in the Sargasso Sea. *Science*, *274*, 1503-1508.

Keigwin, L. D. and Boyle, E. A. (2000). Detecting Holocene changes in thermohaline circulation. *Proceedings of the National Academy of Sciences*, *97*(4), 1343-1346.

Keigwin, L. D. and Boyle, E. A. (2008). Did North Atlantic overturning halt 17,000 years ago? *Paleoceanography*, *23*, PA1101.

Keigwin, L. D. and Jones, G. A. (1989). Glacial-Holocene stratigraphy, chronology, and paleoceanographic observations on some North Atlantic sediment drifts. *Deep Sea Research Part A: Oceanographic Research Papers*, *36*(6), 845-867.

Keigwin, L. D. and Jones, G. A. (1994). Western North Atlantic evidence for millennial-scale changes in ocean circulation and climate. *Journal of Geophysical Research*, *99*(C9), 12,397-12,410.

Keigwin, L. D., Corliss, B. H., Druffel, E. R. M., and Laine, E. P. (1984). High resolution isotope study of the latest deglaciation based on Bermuda Rise cores. *Quaternary Research*, *22*, 383-386.

Keigwin, L. D., Jones, G. A., Lehman, S. J., and Boyle, E. A. (1991). Deglacial meltwater discharge, North Atlantic deep circulation, and abrupt climate change. *Journal of Geophysical Research: Oceans*, *96*(C9), 16,811-16,826.

Laine, E. P., Gardner, W. D., Richardson, M. J., and Kominz, M. (1994). Abyssal currents and advection of resuspended sediment along the northeastern Bermuda Rise. *Marine Geology*, *119*, 159-171.

Lippold, J., Grützner, J., Winter, D., Lahaye, Y., Mangini, A., and Christl, M. (2009). Does sedimentary ^{231}Pa/^{230}Th from the Bermuda Rise monitor past Atlantic Meridional Overturning Circulation? *Geophysical Research Letters*, *36*(12).

Lopes dos Santos, R. A., Prange, M., Castañeda, I. S., Schefub, E., Mulitza, S., Schulz, M., Niedermeyer, E. M., Sinninghe Damasté, J. S., and Schouten, S. (2010). Glacial-interglacial variability in Atlantic meridional overturning circulation and thermocline adjustments in the tropical North Atlantic. *Earth and Planetary Science Letters*, *300*, 407-414.

Luo, S. and Ku, T. L. (1999). Oceanic ^{231}Pa/^{230}Th ratio influenced by particle composition and remineralization. *Earth and Planetary Science Letters*, *167*, 183-195.

Luo, S. and Ku, T. L. (2004). On the importance of opal, carbonate, and lithogenic clays in scavenging and fractionating ^{230}Th, ^{231}Pa and ^{10}Be in the ocean. *Earth and Planetary Science Letters*, *220*, 201-211.

Lynch-Stieglitz, J., Adkins, J. F., Curry, W. B., Dokken, T., Hall, I. R., Herguera, J. C., Hirschi, J. J. M., Ivanova, E. V., Kissel, C., Marchal, O., Marchitto, T. M., McCave, I. N., McManus, J. F., Mulitza, S., Ninnemann, U., Peeters, F., Yu, E. F., and Zahn, R. (2007). Atlantic Meridional Overturning Circulation during the Last glacial Maximum. *Science*, *316*, 66-69.

Mackensen, A., Rudolph, M., and Kuhn, G. (2001). Late Pleistocene deep-water circulation in the subantarctic eastern Atlantic. *Global and Planetary Change*, *30*(3), 197-229.

Maier-Reimer, E., and Mikolajewicz, U. (1989). Experiments with an OGCM on the cause of the Younger Dryas. *Proc. Joint Oceanogr. Assent.*, 87–99.

Marchal, O., Francois, R., Stocker, T. F., and Joos, F. (2000). Ocean thermohaline circulation and sedimentary ^{231}Pa/^{230}Th ratio. *Paleoceanography*, *15*(6), 625-641.

Matsumoto, K. (2007) Radiocarbon-based circulation age of the world oceans. *Journal of Geophysical Research*, *112*(C9).

McCave, I. N. (2002). A Poisoned Chalice? *Science*, *298*, 1186-1187.

McManus, J. F., Francois, R., Gherardi, J. M., Keigwin, L. D., and Brown-Leger, S. (2004). Collapse and rapid resumption of Atlantic meridional circulation linked to deglacial climate changes. *Nature*, *428*, 834-837.

Mortlock, R. A. and Froelich, P. N. (1989). A simple method for the rapid determination of biogenic opal in pelagic marine sediments. *Deep Sea Research, 36*(9), 1425–1426.

Motsumoto, K. (2007). Radiocarbon-based circulation age of the world oceans. *Journal of Geophysical Research: Oceans*, *112*(C9).

Negre, C., Zahn, R., Thomas, A. L., Masqué, P., Henderson, G. M., Martínez-Méndez, G., Hall, I. R., and Mas, J. L. (2010). Reversed flow of Atlantic deep water during the Last Glacial Maximum. *Nature*, *468*, 84-88.

Nozaki, Y., Cochran, J. K., Turekian, K. K., and Keller, G. (1977). Radiocarbon and ^{210}Pb distribution in submersible-taken deep-sea cores from project FAMOUS. *Earth and Planetary Science Letters*, *34*, 167-173.

Rind, D., Peteet, D., Broecker, W., McIntyre, A., and Ruddiman, W. (1986). The impact of cold North Atlantic sea surface temperatures on climate: implications for the Younger Dryas cooling (11-10k). *Climate Dynamics*, *1*(1), 3-33.

Roberts, K. A., Xu, C., Hung, C. C., Conte, M. H., and Santschi, P. H. (2009). Scavenging and fractionation of thorium vs. protactinium in the ocean, as determined from particle-water partitioning experiments with sediment trap material from the Gulf of Mexico and Sargasso Sea. *Earth and Planetary Science Letters*, *286*, 131-138.

Ruddiman, W. F. (2008). Earth’s climate past and future (2nd ed.). New York, NY: W.H. Freeman and Company.

Shemesh, A., Mortlock, R. A., Smith, R. J., and Froelich, P. N. (1988). Determination of Ge/Si in marine siliceous microfossils: Separation, cleaning and dissolution of diatoms and radiolaria. *Marine Chemistry*, *25*(4), 305-323.

Siddall, M., Henderson, G. M., Edwards, N. R., Frank, M., Müller, S. A., Stocker, T. F., and Joos, F. (2005). ^{231}Pa/^{230}Th fractionation by ocean transport, biogenic particle flux and particle type. *Earth and Planetary Science Letters*, *237*, 135-155.

Suman, D. O. and Bacon, M. P. (1989). Variations in Holocene sedimentation in the North American Basin determined from ^{230}Th measurements. *Deep Sea Research*, *36*(6), 869-878.

Vellinga, M. and Wood, R. A. (2002). Global climate impacts of a collapse of the Atlantic thermohaline circulation. *Climate Change*, *54*, 251-267.

Vogt, P. R. and Jung, W. Y. (2007). Origin of the Bermuda volcanoes and Bermuda Rise: history, observations, models, and puzzles. *Geological Society of America Special Papers*, *430*, 553-591.

Walter, H. J., Rutgers van der Loeff, M. M., and Hoeltzen, H. (1997). Enhanced scavenging of ^{231}Pa relative to ^{230}Th in the South Atlantic south of the Polar Front: implications for the use of ^{231}Pa/^{230}Th ratio as a paleoproductivity proxy. *Earth and Planetary Science Letters*, *149*, 85-100.

Yu, E. F., Francois, R., and Bacon, M. P. (1996). Similar rates of modern and last-glacial ocean thermohaline circulation inferred from radiochemical data. *Nature*, *379*, 689-694.

Appendix I: BR-MC2 sediment mass accumulation rates (MAR) based on dry bulk sample masses. Densities are based on 40.53 cm^3 volume (0.5 cm depth, 10.16 cm diameter multicore).

Depth (cm)	Years BP	Total Sample Mass (g)	Density (g/cm^3)	Accumulation (cm/kyr)	MAR (g/cm^2/kyr)
0.0–0.5	0	18.43	0.455	8.292	3.722
0.5–1.0	60	19.76	0.488	8.293	3.845
1.0–1.5	121	18.96	0.468	8.292	3.965
1.5–2.0	181	18.88	0.466	8.293	4.080
2.0–2.5	241	21.02	0.519	8.292	4.191
2.5–3.0	301	19.18	0.473	8.293	4.299
3.0–3.5	362	22.72	0.561	8.292	4.402
3.5–4.0	422	20.71	0.511	8.293	4.502
4.0–4.5	482	20.29	0.501	8.292	4.599
4.5–5.0	543	23.01	0.568	8.293	4.691
5.0–5.5	603	22.74	0.561	8.292	4.780
5.5–6.0	663	23.43	0.578	8.292	4.866
6.0–6.5	724	23.39	0.577	8.293	4.948
6.5–7.0	784	27.00	0.666	8.292	5.027
7.0–7.5	844	23.67	0.584	8.293	5.102
7.5–8.0	904	26.90	0.664	8.292	5.175
8.0–8.5	965	27.33	0.675	8.293	5.244
8.5–9.0	1025	25.61	0.632	8.292	5.310
9.0–9.5	1085	27.01	0.667	8.293	5.373
9.5–10.0	1146	27.20	0.671	8.292	5.434
10.0–10.5	1206	26.53	0.655	8.293	5.491
10.5–11.0	1266	27.19	0.671	8.292	5.546
11.0–11.5	1327	27.97	0.690	8.490	5.731
11.5–12.0	1385	29.57	0.730	8.490	5.781
12.0–12.5	1444	25.71	0.634	8.490	5.829
12.5–13.0	1503	30.59	0.755	8.490	5.874
13.0–13.5	1562	28.86	0.712	8.490	5.917
13.5–14.0	1621	30.36	0.749	8.490	5.957
14.0–14.5	1680	28.03	0.692	8.490	5.995
14.5–15.0	1739	31.16	0.769	8.490	6.031
15.0–15.5	1798	29.54	0.729	8.490	6.064
15.5–16.0	1857	29.47	0.727	8.490	6.095
16.0–16.5	1915	26.28	0.649	8.490	6.125
16.5–17.0	1974	32.29	0.797	8.490	6.152
17.0–17.5	2033	30.38	0.750	8.490	6.177
17.5–18.0	2092	31.09	0.767	8.490	6.201
18.0–18.5	2151	31.10	0.768	8.490	6.222
18.5–19.0	2210	26.37	0.651	8.490	6.242
19.0–19.5	2269	26.50	0.654	8.490	6.260
19.5–20.0	2328	31.87	0.787	8.490	6.277

BR-MC2 sediment mass accumulation rates (continued).

Depth (cm)	Years BP	Total Sample Mass (g)	Density (g/cm^3)	Accumulation (cm/kyr)	MAR (g/cm^2/kyr)
20.0–20.5	2387	29.15	0.719	8.490	6.292
20.5–21.0	2446	30.25	0.746	8.490	6.306
21.0–21.5	2504	29.42	0.726	8.490	6.318
21.5–22.0	2563	26.08	0.644	8.490	6.329
22.0–22.5	2622	30.01	0.741	8.490	6.339
22.5–23.0	2681	25.10	0.619	8.490	6.348
23.0–23.5	2740	28.31	0.699	3.695	2.766
23.5–24.0	2875	30.06	0.742	3.695	2.769
24.0–24.5	3011	29.22	0.721	3.695	2.771
24.5–25.0	3146	27.37	0.675	3.695	2.773
25.0–25.5	3281	32.73	0.808	3.695	2.775
25.5–26.0	3417	23.49	0.580	3.695	2.776
26.0–26.5	3552	30.99	0.765	3.695	2.777
26.5–27.0	3687	30.71	0.758	3.695	2.778
27.0–27.5	3823	30.42	0.751	3.695	2.779
27.5–28.0	3958	32.51	0.802	3.695	2.779
28.0–28.5	4093	31.04	0.766	3.695	2.780
28.5–29.0	4229	32.94	0.813	3.695	2.780
29.0–29.5	4364	33.07	0.816	3.695	2.780
29.5–30.0	4499	37.01	0.913	3.695	2.780
30.0–30.5	4635	30.50	0.753	3.695	2.779
30.5–31.0	4770	29.05	0.717	3.695	2.779
31.0–31.5	4905	29.79	0.735	3.695	2.779
31.5–32.0	5041	24.15	0.596	3.695	2.779
32.0–32.5	5176	46.59	1.150	3.695	2.779
32.5–33.0	5311	28.08	0.693	3.695	2.779
33.0–33.5	5447	30.05	0.742	3.695	2.780
33.5–34.0	5582	26.68	0.659	3.695	2.780
34.0–34.5	5717	30.34	0.749	3.695	2.781
34.5–35.0	5853	29.67	0.732	3.695	2.782
35.0–35.5	5988	35.12	0.867	4.018	3.026
35.5–36.0	6112	28.77	0.710	4.018	3.028
36.0–36.5	6237	32.51	0.802	4.018	3.030
36.5–37.0	6361	31.20	0.770	4.018	3.032
37.0–37.5	6486	27.75	0.685	4.018	3.035
37.5–38.0	6610	29.10	0.718	4.018	3.038
38.0–38.5	6735	33.78	0.834	4.018	3.042
38.5–39.0	6859	33.05	0.816	4.018	3.046
39.0–39.5	6984	33.01	0.815	4.018	3.051
39.5–40.0	7108	27.44	0.677	4.018	3.056

BR-MC2 sediment mass accumulation rates (continued).

Depth (cm)	Years BP	Total Sample Mass (g)	Density (g/cm^3)	Accumulation (cm/kyr)	MAR (g/cm^2/kyr)
40.0–40.5	7232	32.75	0.808	4.018	3.062
40.5–41.0	7357	27.85	0.687	4.018	3.069
41.0–41.5	7481	33.11	0.817	4.018	3.076
41.5–42.0	7606	28.48	0.703	4.018	3.084
42.0–42.5	7730	25.00	0.617	4.018	3.093
42.5–43.0	7855	30.74	0.759	4.018	3.102
43.0–43.5	7979	32.23	0.795	4.018	3.112
43.5–44.0	8103	33.01	0.815	4.018	3.124
44.0–44.5	8228	30.16	0.744	4.018	3.136
44.5–45.0	8352	32.72	0.807	4.018	3.149
45.0–45.5	8477	32.71	0.807	4.018	3.163
45.5–46.0	8601	33.23	0.820	4.018	3.178
46.0–46.5	8726	29.00	0.716	4.018	3.194
46.5–47.0	8850	31.19	0.770	4.018	3.211
47.0–47.5	8975	36.51	0.901	4.018	3.229

Appendix II: BR-MC2 radionuclide data.

Depth (cm)	Years BP	$^{230}Th_{xs}$ (dpm/g)				$^{231}Pa_{xs}$ (dpm/g)		Average Activities (dpm/g)		Average $^{231}Pa_{xs}/^{230}Th_{xs}$
		Batch 1	Batch 2	Batch 3	Batch 4	Batch 3	Batch 4	$^{230}Th_{xs}$	$^{231}Pa_{xs}$	
0.0–0.5	0	3.019	2.918	3.084	3.053	0.156	0.256	3.018	0.206	0.068
2.0–2.5	241				5.425		0.332	5.425	0.332	0.061
3.5–4.0	422				5.783		0.336	5.783	0.336	0.058
7.0–7.5	844				5.553		0.301	5.553	0.301	0.054
8.5–9.0	1025				5.697		0.330	5.697	0.330	0.058
10.5–11.0	1266				6.065		0.335	6.065	0.335	0.055
13.5–14.0	1621		5.332			0.268		5.332	0.268	0.050
28.0–28.5	4093		5.503	5.485		0.265		5.494	0.265	0.048
35.0–35.5	5988		6.068	6.086		0.307		6.077	0.307	0.051
39.0–39.5	6984	6.201	6.329	6.256		0.299		6.262	0.299	0.048
47.0–47.5	8975		5.552	5.876		0.288		5.714	0.288	0.050

Appendix III: BR-MC2 biogenic opal mass accumulation rates (MAR) based on sample accumulation rates from Appendix II.

Depth (cm)	Years BP	Total Sample Mass (g)	Biogenic Opal %	Opal MAR ($g/cm^2/kyr$)
0.0–0.5	0	18.43	2.90	0.110
0.5–1.0	60	19.76	2.50	0.101
1.0–1.5	121	18.96	2.45	0.095
1.5–2.0	181	18.88	2.08	0.080
2.0–2.5	241	21.02	1.99	0.086
2.5–3.0	301	19.18	2.10	0.082
3.0–3.5	362	22.72	1.87	0.087
3.5–4.0	422	20.71	1.88	0.080
4.0–4.5	482	20.29	1.97	0.082
4.5–5.0	543	23.01	2.03	0.096
5.0–5.5	603	22.74	2.07	0.096
5.5–6.0	663	23.43	2.20	0.105
6.0–6.5	724	23.39	2.33	0.112
6.5–7.0	784	27.00	1.97	0.109
7.0–7.5	844	23.67	2.16	0.105
7.5–8.0	904	26.90	2.06	0.114
8.0–8.5	965	27.33	2.18	0.122
8.5–9.0	1025	25.61	2.43	0.127
9.0–9.5	1085	27.01	2.15	0.119
9.5–10.0	1146	27.20	2.32	0.129
10.0–10.5	1206	26.53	2.48	0.135
10.5–11.0	1266	27.19	1.93	0.107
11.0–11.5	1327	27.97	2.39	0.140
11.5–12.0	1385	29.57	2.54	0.158
12.0–12.5	1444	25.71	2.20	0.118
12.5–13.0	1503	30.59	2.69	0.173
13.0–13.5	1562	28.86	2.28	0.138
13.5–14.0	1621	30.36	2.82	0.179
14.0–14.5	1680	28.03	2.60	0.153
14.5–15.0	1739	31.16	2.08	0.136
15.0–15.5	1798	29.54	1.80	0.111
15.5–16.0	1857	29.47	2.45	0.151
16.0–16.5	1915	26.28	2.20	0.121
16.5–17.0	1974	32.29	1.81	0.123
17.0–17.5	2033	30.38	2.31	0.147
17.5–18.0	2092	31.09	1.94	0.126
18.0–18.5	2151	31.10	1.95	0.127
18.5–19.0	2210	26.37	2.38	0.132
19.0–19.5	2269	26.50	1.98	0.110
19.5–20.0	2328	31.87	2.12	0.142

BR-MC2 biogenic opal mass accumulation rates (continued).

Depth (cm)	Years BP	Total Sample Mass (g)	Biogenic Opal %	Opal MAR (g/cm^2/kyr)
20.0–20.5	2387	29.15	1.85	0.113
20.5–21.0	2446	30.25	1.65	0.104
21.0–21.5	2504	29.42	1.90	0.117
21.5–22.0	2563	26.08	1.68	0.092
22.0–22.5	2622	30.01	1.67	0.105
22.5–23.0	2681	25.10	2.17	0.114
23.0–23.5	2740	28.31	1.91	0.049
23.5–24.0	2875	30.06	1.69	0.046
24.0–24.5	3011	29.22	1.97	0.053
24.5–25.0	3146	27.37	1.92	0.048
25.0–25.5	3281	32.73	1.56	0.047
25.5–26.0	3417	23.49	1.72	0.037
26.0–26.5	3552	30.99	1.49	0.042
26.5–27.0	3687	30.71	1.57	0.044
27.0–27.5	3823	30.42	1.84	0.051
27.5–28.0	3958	32.51	1.57	0.047
28.0–28.5	4093	31.04	1.29	0.036
28.5–29.0	4229	32.94	1.97	0.059
29.0–29.5	4364	33.07	1.81	0.055
29.5–30.0	4499	37.01	1.66	0.056
30.0–30.5	4635	30.50	1.65	0.046
30.5–31.0	4770	29.05	1.37	0.036
31.0–31.5	4905	29.79	1.49	0.041
31.5–32.0	5041	24.15	1.33	0.029
32.0–32.5	5176	46.59	1.30	0.055
32.5–33.0	5311	28.08	1.69	0.043
33.0–33.5	5447	30.05	1.40	0.038
33.5–34.0	5582	26.68	1.46	0.035
34.0–34.5	5717	30.34	1.58	0.044
34.5–35.0	5853	29.67	1.47	0.040
35.0–35.5	5988	35.12	1.23	0.043
35.5–36.0	6112	28.77	1.77	0.050
36.0–36.5	6237	32.51	1.76	0.057
36.5–37.0	6361	31.20	1.65	0.051
37.0–37.5	6486	27.75	1.92	0.053
37.5–38.0	6610	29.10	1.80	0.052
38.0–38.5	6735	33.78	1.62	0.054
38.5–39.0	6859	33.05	2.01	0.066
39.0–39.5	6984	33.01	1.84	0.060
39.5–40.0	7108	27.44	2.01	0.055

BR-MC2 biogenic opal mass accumulation rates (continued).

Depth (cm)	Years BP	Total Sample Mass (g)	Biogenic Opal %	Opal MAR (g/cm^2/kyr)
40.0–40.5	7232	32.75	1.41	0.046
40.5–41.0	7357	27.85	1.56	0.043
41.0–41.5	7481	33.11	1.50	0.049
41.5–42.0	7606	28.48	1.40	0.040
42.0–42.5	7730	25.00	1.28	0.032
42.5–43.0	7855	30.74	1.33	0.041
43.0–43.5	7979	32.23	1.38	0.044
43.5–44.0	8103	33.01	1.12	0.037
44.0–44.5	8228	30.16	1.58	0.047
44.5–45.0	8352	32.72	1.34	0.043
45.0–45.5	8477	32.71	1.36	0.044
45.5–46.0	8601	33.23	1.22	0.040
46.0–46.5	8726	29.00	1.70	0.049
46.5–47.0	8850	31.19	1.76	0.055
47.0–47.5	8975	36.51	1.29	0.047

Appendix IV: BR-MC2 stable isotope data.

Depth (cm)	Years BP	$\delta^{18}O_{VPDB}$ ‰	$\delta^{13}C_{VPDB}$ ‰
0.0–0.5	0	-0.378	-0.474
0.5–1.0	60	-0.257	0.237
1.0–1.5	121		
1.5–2.0	181	-0.722	-0.517
2.0–2.5	241	-0.385	-0.346
2.5–3.0	301	-0.341	-0.719
3.0–3.5	362	-0.517	-0.582
3.5–4.0	422	-0.446	-0.258
4.0–4.5	482	-0.602	-0.698
4.5–5.0	543	-1.413	-1.031
5.0–5.5	603	-0.356	-0.525
5.5–6.0	663	-0.564	-0.548
6.0–6.5	724	-0.346	-0.031
6.5–7.0	784	-0.259	-0.590
7.0–7.5	844	-0.737	-0.105
7.5–8.0	904	-0.486	-0.511
8.0–8.5	965	-0.517	-0.661
8.5–9.0	1025	-0.584	-0.714
9.0–9.5	1085	-0.418	-0.236
9.5–10.0	1146	-0.842	-0.947
10.0–10.5	1206	-0.359	-1.141
10.5–11.0	1266	-0.567	-0.520
11.0–11.5	1327	-0.973	-0.144
11.5–12.0	1385	-0.821	-0.404
12.0–12.5	1444	-0.490	-0.233
12.5–13.0	1503	-0.262	-0.484
13.0–13.5	1562	-0.922	-1.269
13.5–14.0	1621	-0.499	-0.412
14.0–14.5	1680	-0.374	0.164
14.5–15.0	1739	-0.412	-0.322
15.0–15.5	1798	-0.482	-1.006
15.5–16.0	1857	-0.762	-1.250
16.0–16.5	1915	-0.343	-0.599
16.5–17.0	1974	-0.613	-0.151
17.0–17.5	2033	-0.708	-0.747
17.5–18.0	2092	-1.017	-0.134
18.0–18.5	2151	-0.811	-0.433
18.5–19.0	2210	-0.702	-0.178
19.0–19.5	2269	-0.822	-0.041
19.5–20.0	2328	-0.936	0.154

BR-MC2 stable isotope data (continued).

Depth (cm)	Years BP	$\delta^{18}O_{VPDB}$ ‰	$\delta^{13}C_{VPDB}$ ‰
20.0–20.5	2387	-0.658	0.307
20.5–21.0	2446	-0.916	0.531
21.0–21.5	2504	-1.165	-0.152
21.5–22.0	2563	-0.686	0.025
22.0–22.5	2622	-0.521	0.227
22.5–23.0	2681	-0.313	0.553
23.0–23.5	2740	-1.068	-0.031
23.5–24.0	2875	-0.539	0.680
24.0–24.5	3011	-0.174	0.256
24.5–25.0	3146		0.756
25.0–25.5	3281	-1.505	-0.266
25.5–26.0	3417	-0.314	
26.0–26.5	3552	-1.091	-0.126
26.5–27.0	3687	-1.176	-0.835
27.0–27.5	3823	-0.965	-0.338
27.5–28.0	3958	-1.130	-0.833
28.0–28.5	4093	-0.886	0.093
28.5–29.0	4229	-1.085	-0.480
29.0–29.5	4364	-1.497	-1.305
29.5–30.0	4499	-0.220	-0.615
30.0–30.5	4635	-0.746	-0.570
30.5–31.0	4770	-0.872	-0.906
31.0–31.5	4905	-0.788	-0.116
31.5–32.0	5041	-1.303	0.501
32.0–32.5	5176	-0.571	-0.712
32.5–33.0	5311	-0.823	0.292
33.0–33.5	5447	-1.415	-0.097
33.5–34.0	5582	-0.771	-1.366
34.0–34.5	5717	-0.647	-0.228
34.5–35.0	5853	-0.723	-0.846
35.0–35.5	5988	-1.136	-0.415
35.5–36.0	6112	-0.482	-0.399
36.0–36.5	6237	-0.507	-0.033
36.5–37.0	6361	-0.825	0.181
37.0–37.5	6486	-0.616	-0.232
37.5–38.0	6610	-0.940	-0.207
38.0–38.5	6735	-0.780	-0.138
38.5–39.0	6859	-0.561	-0.486
39.0–39.5	6984	-0.735	0.152
39.5–40.0	7108	-0.851	-0.417

BR-MC2 stable isotope data (continued).

Depth (cm)	Years BP	$\delta^{18}O_{VPDB}$ ‰	$\delta^{13}C_{VPDB}$ ‰
40.0–40.5	7232	-0.428	-0.420
40.5–41.0	7357	-0.663	-0.502
41.0–41.5	7481	-1.404	-0.167
41.5–42.0	7606	-1.090	-1.003
42.0–42.5	7730	-0.896	-0.987
42.5–43.0	7855	-0.314	-0.579
43.0–43.5	7979	-0.902	0.136
43.5–44.0	8103	-0.649	-0.025
44.0–44.5	8228	-0.859	-0.496
44.5–45.0	8352	-0.748	-0.397
45.0–45.5	8477	-0.700	-0.392
45.5–46.0	8601	-0.696	-0.181
46.0–46.5	8726	-0.795	-0.478
46.5–47.0	8850	-0.574	-0.399
47.0–47.5	8975	-0.574	-0.311